

Adaptive change of basis in entropy-based moment closures for linear kinetic equations

Graham W. Alldredge^{a,1,3,*}, Cory D. Hauck^{b,1}, Dianne P. O'Leary^{c,3}, André L. Tits^{a,3}

^a*Department of Electrical and Computer Engineering & Institute for Systems Research, University of Maryland College Park, MD 20742 USA*

^b*Computational Mathematics Group, Computer Science and Mathematics Division, Oak Ridge National Laboratory, Oak Ridge, TN 37831 USA*

^c*Department of Computer Science, University of Maryland College Park, MD 20742 USA*

Abstract

Entropy-based (M_N) moment closures for kinetic equations are defined by a constrained optimization problem that must be solved at every point in a space-time mesh, making it important to solve these optimization problems accurately and efficiently. We present a complete and practical numerical algorithm for solving the dual problem in one-dimensional, slab geometries. The closure is only well-defined on the set of moments that are realizable from a positive underlying distribution, and as the boundary of the realizable set is approached, the dual problem becomes increasingly difficult to solve due to ill-conditioning of the Hessian matrix. To improve the condition number of the Hessian, we advocate the use of a change of polynomial basis, defined using a Cholesky factorization of the Hessian, that permits solution of problems nearer to the boundary of the realizable set. We also advocate a fixed quadrature scheme, rather than adaptive quadrature, since the latter introduces unnecessary expense and changes the computationally realizable set as the quadrature changes. For very ill-conditioned problems, we use regularization to make the optimization algorithm robust. We design a manufactured solution and demonstrate that the adaptive-basis optimization algorithm reduces the need for regularization. This is important since we also show that regularization slows, and even stalls, convergence of the numerical simulation when refining the space-time mesh. We also simulate two well-known benchmark problems. There we find that our adaptive-basis, fixed-quadrature algorithm uses less regularization than alternatives, although differences in the resulting numerical simulations are more sensitive to the regularization strategy than to the choice of basis.

Keywords: convex optimization, realizability, kinetic theory, transport, entropy-based

*Corresponding author.

Email addresses: `alldredge@mathcces.rwth-aachen.de` (Graham W. Alldredge), `hauckc@ornl.gov` (Cory D. Hauck), `oleary@cs.umd.edu` (Dianne P. O'Leary), `andre@umd.edu` (André L. Tits)

¹Present address: Center for Computational Engineering Science, RWTH-Aachen University, Aachen, Germany

²This author's research was sponsored by the Office of Advanced Scientific Computing Research and performed at the Oak Ridge National Laboratory, which is managed by UT-Battelle, LLC under Contract No. De-AC05-00OR22725.

³Supported by the U.S. Department of Energy, under Grant DESC0001862.

1. Introduction

Moment methods are commonly used to derive reduced models of kinetic transport. Rather than fully resolve the kinetic distribution in phase space, moment models instead track the evolution of a finite number of weighted velocity averages, or moments of the distribution. Exact equations for these moments inevitably require missing information about the unknown kinetic distribution that must be approximated via a closure. Entropy-based closures approximate the full kinetic distribution by an ansatz that solves a constrained, convex optimization problem. In the context of radiative transport [1, 2], these models are commonly referred to as M_N (after G.N. Minerbo), where N is the order of the highest-order moments of the model; see [3] for additional references. These moment models preserve many fundamental properties of the kinetic description, including positivity, entropy dissipation, and hyperbolicity [4].

The primary drawback of the entropy-based approach is computational cost: at least one optimization problem must be solved at every point on a space-time grid and, except for some M_1 cases, the optimization must be done numerically. For some moments, the associated optimization problem can be particularly expensive to solve. These moments lie near the boundary of the *realizable set*, defined as the set of vectors that are moments of a positive distribution. For realizable moments near the boundary, the optimization algorithm may require a large number of iterations to converge (or may not converge at all) and the solution will be sensitive to small changes in the moments. (Indeed, in some contexts, there even are realizable moments for which the optimization problem has no solution [5, 6, 7, 8].)

It is most common to solve each optimization problem via the associated convex dual. For a smooth entropy function, a standard Newton method was proposed in [9]. In this context, the difficulty in solving optimization problems for moments near the realizable boundary is characterized by an ill-conditioned Hessian for the dual objective function. This matrix is a weighted integral in momentum space of a distribution of rank-one matrices. It becomes rank deficient (or nearly so) because the weight function is an approximation of the underlying kinetic density, and for moments near the realizable boundary, its mass will be concentrated around a small number of directions in momentum space. This is a common occurrence in radiation applications. The sensitivity is further exacerbated by the necessity of using an inexact quadrature and finite-precision arithmetic to approximate the integrals. The contributions to the quadrature may effectively be zero for most of the quadrature points, causing the computed Hessian to be singular.

The singularity in the dual Hessian has been addressed in different ways, in particular in the context of some variations of Newton’s method. In [10], the author takes advantage of the structure of the Hessian, whose entries are themselves moments of a known distribution that changes at each iteration. Using orthogonal polynomials with respect to this distribution (which are found using a standard three-point recursion relation [11, Ch. 22]), the author is able to invert the ill-conditioned Hessian in a stable way. (See [12] for an efficient algorithm to evaluate the recursion coefficients.) More recently, orthogonal polynomials were used in the multi-dimensional implementation found in [13, 14]. There the author applies a BFGS

quasi-Newton method (see, e.g., [15, Ch. 6]) and, when the approximate Hessian becomes ill-conditioned, a Gram-Schmidt procedure is applied to change into a polynomial basis for which the Hessian is the identity.⁴ In [16], a penalized version of the primal problem was introduced in order to handle nonrealizable moments. This modification amounts to Tikhonov regularization of the dual problem, which also reduces ill-conditioning of the Hessian for realizable moments that are near the realizable boundary. In [17], two modifications to the Newton method for the solution of the dual problem were introduced. The first, which is only practical for a relatively small number of moments, is to generate an initial guess for the Newton solver by interpolating values from look-up tables. The second, which is only practical in one-dimension, is a root finding algorithm to guide the placement of nodes in the adaptive quadrature used to evaluate the objective function and its derivatives. Finally, in [3], where a damped Newton method is used, ill-conditioning of the Hessian near the realizable boundary is avoided in two ways. First, adaptive quadrature is used to better capture the support of the Hessian weight function and thereby increase the number of significant rank-one contributions. Second, a regularization method is introduced to move the moments away from the realizable boundary. These two remedies are automatically invoked as needed, since manual intervention is impractical.

Several specialized techniques for solving the dual problem have also been suggested. In [18, 19], the authors show that, in the case of the Maxwell-Boltzmann entropy, the solution of the dual problem is the unique solution of a certain finite set of linear equations. Unfortunately, setting up this linear system requires the knowledge of additional moments that are not available to the closure. In [20], the authors solve the dual problem by means of a coordinate descent method, also known as Bregman’s balancing method [21, 22], where each sub-problem is solved using a multiple algebraic reconstruction technique [23, 21]. Coordinate descent, however, is known to converge rather slowly (see, e.g., [15, p.230]).

In this paper, along the lines of [3], we employ a damped Newton method and investigate ways to better handle hard optimization problems near the realizable boundary. We note that adaptive quadrature complicates realizability, so we do not use it. Further, we show that regularization affects accuracy and therefore should be avoided whenever possible. For this, we adopt the change-of-basis procedure introduced in [13, 14], albeit with a different implementation. We focus on the Maxwell-Boltzmann entropy in the one-dimensional setting on a bounded domain, although our methodology is applicable to general smooth entropies and moments defined over bounded domains of arbitrary dimension.

As in [13, 14], we observe that the change of basis makes the optimization more stable and effectively removes the need for an adaptive quadrature. Regularization is still required for robustness but is invoked far less frequently, resulting in noticeable improvements in accuracy in manufactured solution simulations we performed. We perform a series of numerical tests to quantify the overall performance of the algorithm, to assess the interplay between the change of basis and the regularization, and to determine efficient stopping criteria for the optimization. Our tests include a new manufactured solution and two well-known

⁴In contrast to our problem, ill-conditioning in [13, 14] occurs because the moments are integrals over an unbounded domain, so the Hessian is dominated by moments corresponding to the highest order polynomials [5].

benchmarks for transport in slab geometries.

The organization of the paper is as follows. In Section 2, we recall the one-dimensional kinetic equation, the derivation of entropy-based moment models, and the issue of realizability that is central to the challenges of implementation. In Sections 3 and 4, we present our ideas for solving the moment closure problem numerically, including the adaptive change of basis, the use of fixed quadrature, and the strategy for regularization. In Section 5, we give results of numerical experimentation, which analyze the efficiency of different strategies combining the change of basis and the regularization procedure. We also examine the effects of several parameters on algorithm efficiency. Experiments include single optimization problems which explore the realizable boundary, accuracy tests using manufactured solutions, and two common benchmarks tests. Finally, we draw conclusions in Section 6.

2. The Closure Problem

In this section, we provide a brief introduction to the closure problem, following the detailed presentation in [3, 24]. We consider the migration of particles with unit speed that are absorbed by or scattered isotropically off of a background material medium with slab geometry. The particle system is characterized by a non-negative kinetic density $F = F(x, \mu, t)$ that is governed by a kinetic transport equation

$$\partial_t F + \mu \partial_x F + \sigma_t F = \frac{\sigma_s}{2} \langle F \rangle, \quad (1)$$

supplemented by appropriate boundary and initial conditions. The independent variables in (1) are the scalar coordinate $x \in (x_L, x_R)$ along the direction perpendicular to the slab, the cosine $\mu \in [-1, 1]$ of the angle between the x -axis and the direction of particle travel, and time t . Interactions with the material are characterized by non-negative variables $\sigma_s(x)$, $\sigma_a(x)$, and $\sigma_t(x) := \sigma_s(x) + \sigma_a(x)$ which are the scattering, absorption, and total cross-sections, respectively. For the purposes of this paper, these cross-sections are assumed to be isotropic, i.e., independent of μ . The angle brackets on the right-hand side of (1) denote integration over μ , i.e., for any integrable function $g = g(\mu)$,

$$\langle g \rangle := \int_{-1}^1 g(\mu) d\mu. \quad (2)$$

Moment models for (1) are systems of partial differential equations of the form

$$\partial_t \mathbf{u} + \partial_x \mathbf{f}(\mathbf{u}) + \sigma_t \mathbf{u} = \sigma_s Q \mathbf{u}. \quad (3)$$

Solutions $\mathbf{u} = [u_0, u_1, \dots, u_N]^T : \mathbb{R} \times (0, \infty) \rightarrow \mathbb{R}^{N+1}$ of (3) provide an approximation to the moments of F with respect to linearly independent functions of μ , i.e., $\mathbf{u}(x, t) \simeq \langle \mathbf{m} F(x, \cdot, t) \rangle$, where $\mathbf{m}(\mu) = [m_0(\mu), m_1(\mu), \dots, m_N(\mu)]^T$. While other choices are possible, we follow standard practice [25] and set m_ℓ to be the ℓ^{th} Legendre polynomial, normalized such that $\langle m_\ell m_{\ell'} \rangle = 2\delta_{\ell, \ell'} / 2(\ell + 1)$. With this choice, the $(N + 1) \times (N + 1)$ matrix Q is given by $Q_{\ell, \ell'} = \delta_{\ell, \ell'} \delta_{\ell, 0}$, so that $Q \mathbf{u} = [u_0, 0, \dots, 0]^T$.

The flux \mathbf{f} is determined by a closure. For entropy-based models,

$$\mathbf{f}(\mathbf{u}) := \langle \mu \mathbf{m} G_{\hat{\alpha}(\mathbf{u})} \rangle \quad (4)$$

whenever \mathbf{u} is “realizable” (defined below), where $G_{\hat{\alpha}(\mathbf{u})}$ is an ansatz for the underlying kinetic distribution and solves the constrained, strictly convex optimization problem

$$\underset{g \in L_+^1(d\mu)}{\text{minimize}} \quad \langle \eta(g) \rangle \quad \text{subject to} \quad \langle \mathbf{m}g \rangle = \mathbf{u}. \quad (5)$$

Here the kinetic entropy density $\eta: \mathbb{R} \rightarrow \mathbb{R}$ is strictly convex and $L_+^1(d\mu)$ is the set of all non-negative, integrable functions with respect to the Lebesgue measure $d\mu$.

The ansatz $G_{\hat{\alpha}(\mathbf{u})}$ belongs to a family of functions that are parameterized by $\alpha \in \mathbb{R}^{N+1}$ and take the form $G_\alpha(\mu) = \eta'_*(\alpha^T \mathbf{m}(\mu))$, where $\eta_*: \mathbb{R} \rightarrow \mathbb{R}$ is the Legendre dual of η and prime denotes differentiation. The Lagrange multipliers $\hat{\alpha}(\mathbf{u})$ solve the unconstrained, strictly convex, dual problem

$$\hat{\alpha}(\mathbf{u}) = \underset{\alpha \in \mathbb{R}^{N+1}}{\text{argmin}} \left\{ \langle \eta_*(\alpha^T \mathbf{m}) \rangle - \alpha^T \mathbf{u} \right\}. \quad (6)$$

(See [4] for more details.) For the purposes of this paper, we focus on the Maxwell-Boltzmann entropy $\eta(z) = z \log(z) - z$. Thus $\eta_*(y) = \eta'_*(y) = e^y$ and

$$G_\alpha = \exp(\alpha^T \mathbf{m}). \quad (7)$$

Problem (6) does have a (unique) solution whenever \mathbf{u} is realizable, in the following sense.

Definition 1. A vector $\mathbf{v} \in \mathbb{R}^{N+1}$ is said to be realizable (with respect to \mathbf{m}) if there exists a function $g \in L_+^1(d\mu)$ such that $\langle \mathbf{m}g \rangle = \mathbf{v}$. The set of all realizable vectors is denoted by $\mathcal{R}_{\mathbf{m}}$.

The set $\mathcal{R}_{\mathbf{m}}$ is an open, pointed, convex cone, and in the one-dimensional setting is characterized by the positive-definiteness of Hankel matrices [26]. For the model problem considered here, $\hat{\alpha}(\mathbf{u})$ is a diffeomorphism from $\mathcal{R}_{\mathbf{m}}$ onto \mathbb{R}^{N+1} . (See [5, 27, 9].) Moments on the boundary of realizability $\partial \mathcal{R}_{\mathbf{m}}$ are uniquely realized by atomic measures—i.e., on the boundary of realizability, the kinetic distribution is a sum of delta functions [28].

A numerical method for solving (3) must preserve $\mathcal{R}_{\mathbf{m}}$. To this end, a finite-volume kinetic scheme was introduced in [3], which takes the semi-discrete form

$$\partial_t \mathbf{u}_j + \frac{\langle \mu \mathbf{m} G_{j+1/2} \rangle - \langle \mu \mathbf{m} G_{j-1/2} \rangle}{\Delta x} + \sigma_t \mathbf{u}_j = \sigma_s Q \mathbf{u}_j, \quad (8)$$

where \mathbf{u}_j , for $j \in \{1, \dots, N_x\}$, approximates the cell average $\mathbf{u}(x, t)$ over an interval $I_j = (x_{j-1/2}, x_{j+1/2}) \subset (x_L, x_R)$ and $G_{j\pm 1/2}$ is an approximation of the entropy ansatz at the cell edge $x_{j\pm 1/2}$ based on a linear reconstruction of $G_j = G_{\hat{\alpha}(\mathbf{u}_j)}$ and a standard minmod-type limiter. Time integration is performed using the second-order strong-stability-preserving Runge-Kutta (SSP-RK2) method [29], also known as Heun’s method or the improved Euler method. This is a two-stage method and thus requires the dual problem (6) to be solved twice for every unknown in space and time. SSP integrators are used because, under appropriate conditions, they preserve convex sets. We let \mathbf{u}_j^n denote the numerical solution at time step n in cell j for $n \in \{0, \dots, N_t\}$. The boundary conditions are implemented by prescribing realizable moments in ghost cells indexed by $j \in \{-1, 0, N_x + 1, N_x + 2\}$ at each stage of the Runge Kutta method.

3. Basics of the Optimization

We focus in this section on components for efficiently solving the dual problem (6). Because the objective is smooth, unconstrained, and strictly convex, we use Newton's method, stabilized by an Armijo backtracking line search [30]. Our optimization algorithm computes an approximation $\bar{\alpha}$ to the true solution $\hat{\alpha}$. The dual objective function $f : \mathbb{R}^{N+1} \rightarrow \mathbb{R}$ is

$$f(\alpha) := \langle G_\alpha \rangle - \alpha^T \mathbf{u}. \quad (9)$$

Its gradient $\mathbf{g} : \mathbb{R}^{N+1} \rightarrow \mathbb{R}^{N+1}$ and Hessian $H : \mathbb{R}^{N+1} \rightarrow \mathbb{R}^{(N+1) \times (N+1)}$ are given by (recall (7))

$$\mathbf{g}(\alpha) := \langle \mathbf{m} G_\alpha \rangle - \mathbf{u} \quad \text{and} \quad H(\alpha) := \langle \mathbf{m} \mathbf{m}^T G_\alpha \rangle, \quad (10)$$

and the Newton direction $\mathbf{d}(\alpha)$ solves the linear system $H(\alpha)\mathbf{d}(\alpha) = -\mathbf{g}(\alpha)$.

Our optimization algorithm has four important components: an adaptive change of basis to improve the conditioning of the Hessian, appropriate stopping criteria, a fixed quadrature set for approximating integrals, and a regularization method used for very ill-conditioned problems. We now consider each of these components.

3.1. Adaptive change of basis

Following [13], we apply a change of basis to improve the condition number of the Hessian. Specifically, when expressed in the new basis, the Hessian at the current iterate becomes the identity matrix. In [13], a BFGS algorithm is used, and the change of basis is invoked only when the condition number of the approximate Hessian is greater than a certain threshold. Here we use a damped Newton method, and we invoke such change of basis at every iteration.

At iteration k , let S_k be an invertible matrix which determines a new polynomial basis $\mathbf{p}_k = S_k \mathbf{m}$ and let $T_k = S_k^{-1}$. If α_k is the dual variable at iteration k with respect to basis \mathbf{m} , then let $\beta_{k,\text{in}} = T_k^T \alpha_k$ be the dual variable at iteration k with respect to basis \mathbf{p}_{k-1} and $\beta_{k,\text{out}} = T_k^T \alpha_k$ be the dual variable at iteration k after changing to the new basis \mathbf{p}_k .

Define a new objective $f_k : \mathbb{R}^{N+1} \rightarrow \mathbb{R}$ by

$$f_k(\beta) := f(S_k^T \beta) = \langle \exp(\beta^T S_k \mathbf{m}) \rangle - \beta^T S_k \mathbf{u}, \quad (11)$$

so that $f(\alpha) = f_k(T_k^T \alpha)$ for all α . Then f_k is strictly convex with gradient and (positive-definite) Hessian

$$\mathbf{g}_k(\beta) = S_k \mathbf{g}(S_k^T \beta) \quad \text{and} \quad H_k(\beta) = S_k H(S_k^T \beta) S_k^T. \quad (12)$$

The Newton step \mathbf{d}_k for f_k at β solves $H_k(\beta)\mathbf{d}_k(\beta) = -\mathbf{g}_k(\beta)$.

Clearly $H_k(\beta_{k,\text{out}}) = I$ if and only if T_k factors $H(\alpha_k)$, i.e., $H(\alpha_k) \equiv H(S_k^T \beta_{k,\text{out}}) = T_k T_k^T$, in which case the Newton direction with respect to \mathbf{p}_k coincides with the steepest descent direction:

$$\mathbf{d}_k(\beta_{k,\text{out}}) = -\mathbf{g}_k(\beta_{k,\text{out}}) = \mathbf{u}_k - \langle \mathbf{p}_k \exp(\beta_{k,\text{out}}^T \mathbf{p}_k) \rangle, \quad (13)$$

where $\mathbf{u}_k = S_k \mathbf{u} = \langle \mathbf{p}_k G_{\hat{\alpha}(\mathbf{u})} \rangle$ is the moment vector expressed in the \mathbf{p}_k basis. Furthermore, \mathbf{p}_k is orthonormal with respect to the weight $G_{\alpha_k} = \exp(\alpha_k^T \mathbf{m}) = \exp(\beta_{k,\text{out}}^T \mathbf{p}_k)$, since

$$\langle \mathbf{p}_k \mathbf{p}_k^T \exp(\alpha_k^T \mathbf{m}) \rangle = S_k \langle \mathbf{m} \mathbf{m}^T \exp(\alpha_k^T \mathbf{m}) \rangle S_k^T = S_k H(\alpha_k) S_k^T = H_k(\beta_{k,\text{out}}) = I. \quad (14)$$

If $H(\boldsymbol{\alpha}_k)$ is ill-conditioned, then a direct computation and application of T_k may be inaccurate. It is more stable to change bases iteratively. To this end, let L_k be any matrix such that

$$H_{k-1}(\boldsymbol{\beta}_{k,\text{in}}) = L_k L_k^T. \quad (15)$$

Using this formula, it is a simple exercise to show that $T_k = T_{k-1} L_k$ factors $H(\boldsymbol{\alpha}_k)$, that $\boldsymbol{\beta}_{k,\text{out}} = L_k^T \boldsymbol{\beta}_{k,\text{in}}$, and that $\mathbf{u}_k = L_k^{-1} \mathbf{u}_{k-1}$.

In exact arithmetic, this change of basis has no effect on the sequence of Newton iterates $\boldsymbol{\alpha}_k$. Using inexact arithmetic, however, we observed (see section 5 below) that when \mathbf{u} is near the realizability boundary, under the proposed change of basis, the stability of the iteration is greatly improved: the Hessian matrix $H(\boldsymbol{\alpha}_k)$ in the original basis is highly ill-conditioned, so performing matrix computations with L_k and T_k —whose condition numbers are the square root of those of $H_{k-1}(\boldsymbol{\beta}_{k,\text{in}})$ and $H(\boldsymbol{\alpha}_k)$ respectively—instead of with $H(\boldsymbol{\alpha}_k)$ should reduce errors. Furthermore, when the Hessian matrix in the original basis is poorly conditioned, the computed Newton direction may even fail to be a direction of descent for the objective function. In contrast, in the new coordinate system, the step is taken in the direction of the negative of the computed gradient. Even in inexact arithmetic this computed step is quite likely to have a negative inner product with the true gradient and thus be a descent direction.

3.2. Stopping the Newton iteration

Following [3], our stopping criterion involves two conditions:

$$\|\mathbf{g}(\boldsymbol{\alpha}_k)\|_2 \leq \tau \quad \text{and} \quad \exp(5\|\mathbf{d}(\boldsymbol{\alpha}_k)\|_1) \leq 1 + \varepsilon_\gamma. \quad (16)$$

In view of (10), the first condition bounds the Euclidean distance between \mathbf{u} and the moments of the candidate ansatz $G_{\boldsymbol{\alpha}_k}$. Moreover, because the spectral radius of the Jacobian of \mathbf{f} is bounded by one [31], it also bounds the error in the flux \mathbf{f} (see (4), (7)):

$$\|\mathbf{f}(\mathbf{u}) - \langle \mu \mathbf{m} G_{\boldsymbol{\alpha}_k} \rangle\|_2 \leq \sup_{\mathbf{v} \in \mathcal{R}_{\mathbf{m}}} \left\| \frac{\partial \mathbf{f}}{\partial \mathbf{v}}(\mathbf{v}) \right\|_2 \|\mathbf{u} - \langle \mathbf{m} G_{\boldsymbol{\alpha}_k} \rangle\|_2 \leq \|\mathbf{g}(\boldsymbol{\alpha}_k)\|_2 \quad (17)$$

The second condition estimates an upper bound on

$$\gamma(\mu) := G_{\boldsymbol{\alpha}_k} / G_{\hat{\boldsymbol{\alpha}}(\mathbf{u})} = G_{\boldsymbol{\alpha}_k - \hat{\boldsymbol{\alpha}}(\mathbf{u})}, \quad (18)$$

the ratio of the ansatz associated with a current iterate $\boldsymbol{\alpha}_k$ to the ansatz of the solution $\hat{\boldsymbol{\alpha}}(\mathbf{u})$. The purpose of this condition (see Theorem 1 below) is to maintain realizability of the moments generated by the kinetic scheme in Section 2. Following [3], we use the Newton direction $\mathbf{d}(\boldsymbol{\alpha}_k)$ to approximate $\boldsymbol{\alpha}_k - \hat{\boldsymbol{\alpha}}(\mathbf{u})$, but rather than the two-norm estimate used in [3], we use a tighter estimate to bound $G_{\mathbf{d}(\boldsymbol{\alpha}_k)}$:

$$\max_{\mu \in [-1, 1]} G_{\mathbf{d}(\boldsymbol{\alpha}_k)} = \max_{\mu \in [-1, 1]} \exp(\mathbf{d}(\boldsymbol{\alpha}_k)^T \mathbf{m}) \leq \exp(\|\mathbf{d}(\boldsymbol{\alpha}_k)\|_1), \quad (19)$$

where we have used the fact that $\max_\mu |m_i| = 1$ for all i . Adding a safety factor of 5 gives (16), which ensures with high confidence that

$$\gamma(\mu) \leq 1 + \varepsilon_\gamma. \quad (20)$$

3.3. Fixed Curtis-Clenshaw quadrature

The integrals in the objective function (cf. (9)) and its gradient and Hessian (cf. (10)) cannot, in general, be computed explicitly. Therefore a numerical quadrature rule must be used. Let \mathcal{Q} be a quadrature rule defined for functions $g : [-1, 1] \rightarrow \mathbb{R}$ by

$$\mathcal{Q}(g) = \sum_{i=1}^{n_{\mathcal{Q}}} w_i g(\mu_i), \quad (21)$$

where the quadrature nodes $\{\mu_i\}_{i=1}^{n_{\mathcal{Q}}}$ and the quadrature weights $\{w_i\}_{i=1}^{n_{\mathcal{Q}}}$ are chosen so that $\mathcal{Q}(g)$ approximates $\langle g \rangle$. For numerical computations, $\langle \cdot \rangle$ should always be understood as $\mathcal{Q}(\cdot)$. The specific meaning should be clear from the context. We define the \mathcal{Q} -realizable set

$$\mathcal{R}_{\mathbf{m}}^{\mathcal{Q}} := \left\{ \mathbf{u} \mid \mathbf{u} = \sum_{i=1}^{n_{\mathcal{Q}}} w_i \mathbf{m}(\mu_i) f_i, f_i > 0 \right\}. \quad (22)$$

Note that $\mathcal{R}_{\mathbf{m}}^{\mathcal{Q}}$ is a *strict* (polytopic) subset of $\mathcal{R}_{\mathbf{m}}$ and that, like $\mathcal{R}_{\mathbf{m}}$, it is an open, pointed, convex cone. In particular

$$\mathcal{R}_{\mathbf{m}}^{\mathcal{Q}} = \left\{ \mathbf{u} \mid \mathbf{u} = c\mathbf{v}, c > 0, \mathbf{v} \in \mathcal{R}_{\mathbf{m}}^{\mathcal{Q}}|_{u_0=1} \right\}. \quad (23)$$

In [3], an adaptive quadrature was used to reduce the condition number of the Hessian. However, the use of an adaptive quadrature introduces serious numerical difficulties. For example, the \mathcal{Q} -realizable set changes with the choice of quadrature nodes. Thus an iterate that is realizable can suddenly become non-realizable when the quadrature changes, and this forces the use of artificial techniques like regularization, discussed below, in order to continue the computation. In contrast, a fixed quadrature \mathcal{Q} makes it easy to keep the numerical solution within the \mathcal{Q} -realizable set.

Theorem 1. *Let \mathbf{u}_j^{n+1} , $j \in \{1, \dots, N_x\}$, be defined via the kinetic scheme in Section 2, with time-step restriction*

$$\gamma_{\max} \frac{\Delta t}{\Delta x} \frac{\theta + 2}{2} + \sigma_t \Delta t < 1, \quad (24)$$

and let γ_{\max} be the maximum value of $\gamma(\mu_i)$ (cf. (18)) over all quadrature nodes, spatial cells, and stages of the Runge-Kutta method used to integrate the kinetic scheme in time. If $\mathbf{u}_j^n \in \mathcal{R}_{\mathbf{m}}^{\mathcal{Q}}$ for $j \in \{-1, \dots, N_x + 2\}$ and if the moments in the ghost cells are in $\mathcal{R}_{\mathbf{m}}^{\mathcal{Q}}$ at each stage of the Runge-Kutta scheme, then $\mathbf{u}_j^{n+1} \in \mathcal{R}_{\mathbf{m}}^{\mathcal{Q}}$ for $j \in \{1, \dots, N_x\}$.

The proof of Theorem 1 is a trivial modification of the proof of Theorem 2.5 in [3].

It has also been observed that the size of the error in many adaptive quadrature rules does not decrease monotonically with the number of points and, furthermore, that the number of points required to satisfy a tolerance criterion is often much larger than the number of points needed for an accurate evaluation of the integral [32]. These issues lead to a considerable increase in the complexity and computational time of the optimization algorithm. Moreover, as shown in [3], refining the quadrature does not help if the exact Hessian is ill-conditioned. With the adaptive basis, the condition number of the Hessian is kept under control by

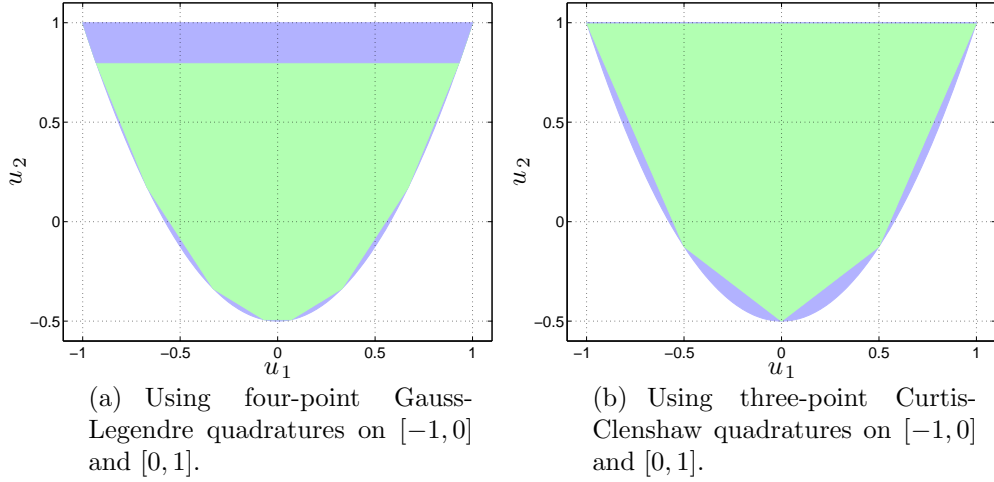


Figure 1: Illustrating $\mathcal{R}_{\mathbf{m}}^{\mathcal{Q}}|_{u_0=1}$ for M_2 . The green indicates $\mathcal{R}_{\mathbf{m}}^{\mathcal{Q}}|_{u_0=1}$, and the blue indicates $\mathcal{R}_{\mathbf{m}}|_{u_0=1} \setminus \mathcal{R}_{\mathbf{m}}^{\mathcal{Q}}|_{u_0=1}$. Ideally, the two sets would coincide.

iteratively changing the polynomial basis. Thus we opt to use a fixed quadrature and avoid the above numerical complications.

Although the dual problem (6) has a solution for all $\mathbf{u} \in \mathcal{R}_{\mathbf{m}}$, the use of a quadrature-based *approximation* of the dual objective function means there will be a solution if and only if $\mathbf{u} \in \mathcal{R}_{\mathbf{m}}^{\mathcal{Q}}$. Consequently, it is important to choose quadratures \mathcal{Q} for which $\mathcal{R}_{\mathbf{m}} \setminus \mathcal{R}_{\mathbf{m}}^{\mathcal{Q}}$ is small. In light of (23), the following characterization of $\mathcal{R}_{\mathbf{m}}^{\mathcal{Q}}|_{u_0=1}$ helps guide this choice.

Proposition 1. *For any quadrature \mathcal{Q} using positive weights w_i ,*

$$\mathcal{R}_{\mathbf{m}}^{\mathcal{Q}}|_{u_0=1} = \text{int co}\{\mathbf{m}(\mu_i)\}_{i=1}^{n_{\mathcal{Q}}}, \quad (25)$$

where *co* indicates the convex hull and *int* the interior.

Proof. Let $\mathbf{u} \in \mathcal{R}_{\mathbf{m}}^{\mathcal{Q}}|_{u_0=1}$. Then, from (22), $\mathbf{u} = \sum \lambda_i \mathbf{m}(\mu_i)$, with $\lambda_i := w_i f_i > 0$. Also, $\sum \lambda_i = 1$ since $u_0 = 1$ and $m_0 \equiv 1$, and therefore $\mathbf{u} \in \text{int co}\{\mathbf{m}(\mu_i)\}$. On the other hand, if $\mathbf{u} \in \text{int co}\{\mathbf{m}(\mu_i)\}$, there must exist scalars λ_i such that $\mathbf{u} = \sum \lambda_i \mathbf{m}(\mu_i)$, with $\lambda_i > 0$ and $\sum \lambda_i = 1$. Choosing $f_i := \lambda_i / w_i$ shows that $\mathbf{u} \in \mathcal{R}_{\mathbf{m}}^{\mathcal{Q}}|_{u_0=1}$. \square

It remains to select a quadrature rule. Figure 1 shows examples of $\mathcal{R}_{\mathbf{m}}^{\mathcal{Q}}$ in the M_2 case ($\mathbf{m} = [1, \mu, \frac{1}{2}(3\mu^2 - 1)]^T$) using low-order Curtis-Clenshaw and Gauss-Legendre quadrature rules. For this choice of \mathbf{m} , $\mathcal{R}_{\mathbf{m}}|_{u_0=1}$ is flat on the top, but curved at the bottom. If the endpoints $\mu = \pm 1$ are nodes of \mathcal{Q} , as in the case of Curtis-Clenshaw quadrature, the entire flat portion at the top is in $\partial \mathcal{R}_{\mathbf{m}}^{\mathcal{Q}}|_{u_0=1}$ (cf. Figure 1(b)). The Gauss-Legendre quadrature, on the other hand, does not contain the endpoints and, as a consequence, leaves large regions of $\mathcal{R}_{\mathbf{m}}$ out of $\mathcal{R}_{\mathbf{m}}^{\mathcal{Q}}$ (cf. Figure 1(a)). With Curtis-Clenshaw, $\mathcal{R}_{\mathbf{m}}^{\mathcal{Q}}$ contains all realizable moments for which $|u_1|/u_0$ is arbitrarily close to one. Such moments occur in many situations, including the plane source benchmark problem simulated in Section 5. These observations motivate our use of Curtis-Clenshaw quadrature rather than Gauss-Legendre quadrature which was used, for example, in [3, 9].

3.4. Regularization

Even with the adaptive basis, there are realizable moments for which the damped Newton method does not converge in a reasonable number of iterations. Indeed $H_{k-1}(\boldsymbol{\beta}_{k,\text{in}})$ can be

highly ill-conditioned even though in the previous step $H_{k-1}(\beta_{k-1,\text{out}}) = I$. In extreme situations, this may cause the factorization in (15) to fail because of round-off errors or to be so inaccurate that the next Newton step is not a descent direction. In the latter case, it is possible to refactor $H_{k-1}(\beta_{k,\text{in}})$ (see Section 4.1) in order to find a descent direction. However, refactorization may be required many times.

To address this issue, we employ the regularization scheme introduced in [3]. The regularization strategy is simple: moments \mathbf{u} for which the dual problem (6) is deemed too difficult to solve (by some prescribed criteria) are replaced by nearby moments $\mathbf{v}(\mathbf{u}, r)$ that are further away from the boundary. These nearby moments are computed by taking the convex combination of \mathbf{u} with the moments of the isotropic distribution with the same particle density:

$$\mathbf{v}(\mathbf{u}, r) := (1 - r)\mathbf{u} + rQ\mathbf{u} \quad (26)$$

where $0 < r \ll 1$. When \mathbf{u} is near $\partial\mathcal{R}_{\mathbf{m}}$, $\hat{\alpha}(\mathbf{v}(\mathbf{u}, r))$ is typically much easier to compute than $\hat{\alpha}(\mathbf{u})$, even for small values of r .

The regularization procedure does introduce errors of order r in the numerical solution. However, with adaptive change of basis, the need for regularization is reduced relative to the fixed-basis method (which was used in [3]).

4. Implementation Issues

Now that we have a broad outline for our optimization algorithm we discuss the implementation details. The complete algorithm is presented in Algorithm 1.

4.1. Defining the orthonormal basis

There are many different orthogonal polynomial bases with respect to $G_{\alpha}d\mu$. In [13], orthogonal bases are computed in which each basis polynomial has the same degree. Indeed, because in [13] the integration domain is unbounded, components of the dual variable associated with basis polynomials of higher polynomial degrees are much more sensitive than those associated to lower degrees. In contrast, the domain of μ in the current application is bounded; hence a triangular basis $\mathbf{p}_k = [p_{k,0}, p_{k,1}, \dots, p_{k,N}]^T$, where the polynomial $p_{k,\ell}$ has degree ℓ , does not present the same numerical difficulties. Rather, in this case, such a basis is preferable since it leads to simpler matrix operations. In addition, since $p_{k,0}$ is a constant, orthogonality of the basis \mathbf{p}_k with respect to G_{α_k} implies that $\langle p_{k,\ell} G_{\alpha_k} \rangle = 0$ for $\ell > 0$. This simplifies the computation of the gradient \mathbf{g}_k (see (13)).

The simplest way to maintain a triangular basis is to let L_k in (15), which defines the iterative change of basis, be the Cholesky factor of $H_{k-1}(\beta_{k,\text{in}})$, i.e., be lower triangular and positive-definite. The steps to orthonormalize the basis using the Cholesky factor are given in Algorithm 2, which at each iteration computes the new multipliers $\beta_{k,\text{out}}$, moments \mathbf{u}_k , gradient \mathbf{g}_k of the dual objective function, the $(N+1) \times n_Q$ matrix P_k of values of the basis polynomials at the quadrature nodes, and the change of basis T_k . Once a triangular basis is initialized, the successive bases \mathbf{p}_k remain triangular, and an initial triangular orthogonal basis is easily available: If we start at the multipliers $\alpha_{\text{iso}} = (\log(u_0/2), 0, \dots, 0)^T$ associated with the isotropic distribution, then the Legendre basis \mathbf{m} (which indeed is triangular) is a natural choice because it is orthogonal with respect to the isotropic ansatz $G_{\alpha_{\text{iso}}}$.

Algorithm 1 The optimization algorithm with regularization.

Input: $\mathbf{u} \in \mathcal{R}_{\mathbf{m}} \subset \mathbb{R}^{N+1}$, $\boldsymbol{\beta}_{0,\text{in}} \in \mathbb{R}^{N+1}$, $T_{-1} \in \mathbb{R}^{(N+1) \times (N+1)}$ *{ \mathbf{u} is assumed to be in the Legendre basis \mathbf{m} , while $\boldsymbol{\beta}_{0,\text{in}}$ is assumed to be in the $\mathbf{p}_{-1} = T_{-1}^{-1}\mathbf{m}$ basis}*

Parameters: $\tau > 0$, $\varepsilon_\gamma > 0$, $k_0 \in \mathbb{N}$, $\xi \in (0, 1/2)$, $\chi \in (0, 1)$, $k_{\max} \in \mathbb{N}$, $\{r_\ell\} \subset [0, 1]$, an increasing sequence starting at zero, $\varepsilon > 0$, \mathcal{Q} , a quadrature rule.

$r_{\max} \leftarrow \max\{r_\ell\}$

for $r \in \{r_\ell\}$ **do**

$P_{-1} \leftarrow T_{-1}^{-1}\mathbf{m}$

$\mathbf{v} \leftarrow ((1-r)\mathbf{u} + r\mathcal{Q}\mathbf{u})$

$\mathbf{v}_{-1} \leftarrow T_{-1}^{-1}\mathbf{v}$

$f_0 \leftarrow \mathcal{Q}(\exp(\boldsymbol{\beta}_{0,\text{in}}^T \mathbf{p}_{-1})) - \boldsymbol{\beta}_{0,\text{in}}^T \mathbf{v}_{-1}$

for $k \in \{0, 1, 2, \dots, k_{\max}\}$ **do**

$[\text{chol_flag}, \boldsymbol{\beta}_{k,\text{out}}, \mathbf{v}_k, \mathbf{g}_k, P_k, T_k] \leftarrow \text{change_basis}(\boldsymbol{\beta}_{k,\text{in}}, \mathbf{v}_{k-1}, P_{k-1}, T_{k-1})$

if $\text{chol_flag} = \text{false}$ and $r = r_{\max}$ **then**

return failure to converge

end if

if $(k > k_0$ or $\text{chol_flag} = \text{false})$ and $r < r_{\max}$ **then**

{Exit the inner for loop so that r is increased.}

break for

else

$e_k \leftarrow \|\mathcal{Q}(\mathbf{m} \exp(\boldsymbol{\beta}_{k,\text{out}}^T T_k^{-1} \mathbf{m})) - \mathbf{v}\|$

$\mathbf{d}_k \leftarrow -\mathbf{g}_k$

if $e_k < \tau$ and $\exp(5\|T_k^{-T} \mathbf{d}_k\|_1) < 1 + \varepsilon_\gamma$ **then**

$\bar{\boldsymbol{\alpha}} \leftarrow T_k^{-T} \boldsymbol{\beta}_{k,\text{out}}$

return $\bar{\boldsymbol{\alpha}}, T_k$

else

$\zeta_k \leftarrow 1$

$\boldsymbol{\beta}_{k+1,\text{in}} \leftarrow \boldsymbol{\beta}_{k,\text{out}}$

while $\zeta_k > \varepsilon \|\boldsymbol{\beta}_{k,\text{out}}\| / \|\mathbf{d}_k\|$ **do**

$f \leftarrow \mathcal{Q}(\exp((\boldsymbol{\beta}_{k,\text{out}} + \zeta_k \mathbf{d}_k)^T \mathbf{p}_k)) - (\boldsymbol{\beta}_{k,\text{out}} + \zeta_k \mathbf{d}_k)^T \mathbf{v}_k$

if $f \leq f_k + \xi \zeta_k \mathbf{g}_k^T \mathbf{d}_k$ **then**

$\boldsymbol{\beta}_{k+1,\text{in}} \leftarrow \boldsymbol{\beta}_{k,\text{out}} + \zeta_k \mathbf{d}_k$

$f_{k+1} \leftarrow f$

break while

end if

$\zeta_k \leftarrow \chi \zeta_k$

end while

end if

end for

end for

return failure to converge

Algorithm 2 The `change_basis` steps used to produce an orthonormal basis using the Cholesky factorization.

Input: $\beta_{\text{in}} \in \mathbb{R}^{N+1}$, $\mathbf{u}_{\text{in}} \in \mathbb{R}^{N+1}$, $P_{\text{in}} \in \mathbb{R}^{(N+1) \times n_Q}$, $T_{\text{in}} \in \mathbb{R}^{(N+1) \times (N+1)}$
{ The Hessian is initially in the \mathbf{p}_{in} basis,⁵ and values of these polynomials at the quadrature nodes are stored in P_{in} . }
 $H \leftarrow \mathcal{Q}(\mathbf{p}_{\text{in}} \mathbf{p}_{\text{in}}^T \exp(\beta_{\text{in}}^T \mathbf{p}_{\text{in}})).$
 $(L, \text{chol_flag}) \leftarrow \text{chol}(H)$ *{chol_flag is false if the Cholesky factorization fails}*
if `chol_flag` = false **then**
 return `chol_flag`, 0, 0, 0, 0, 0
end if
 $P_{\text{out}} \leftarrow L^{-1} P_{\text{in}}$
 $T_{\text{out}} \leftarrow T_{\text{in}} L$
 $\beta_{\text{out}} \leftarrow L^T \beta_{\text{in}}$
 $\mathbf{u}_{\text{out}} \leftarrow L^{-1} \mathbf{u}_{\text{in}}$
 $\mathbf{g}_{\text{out}} \leftarrow (p_{0,\text{out}} \mathcal{Q}(\exp(\beta_{\text{out}}^T \mathbf{p}_{\text{out}})), 0, \dots, 0)^T - \mathbf{u}_{\text{out}}$
return `chol_flag`, β_{out} , \mathbf{u}_{out} , \mathbf{g}_{out} , P_{out} , T_{out}

In exact arithmetic and when applied to the same original basis, Cholesky and modified Gram-Schmidt (used in [13]) both yield the same new basis, up to multiplication of individual basis polynomials by ± 1 . We chose the Cholesky method because it is less computationally expensive than Gram-Schmidt and, in fact, would be recommended in computing the Newton step even if no change of basis was performed. Considering only the highest-order terms, the Cholesky method uses $n_Q N^2/2$ multiplications to form the Hessian, $N^3/6$ multiplications to factor the Hessian, and $n_Q N^2/2$ multiplications to update the array storing the evaluation of the basis polynomials at the quadrature nodes. In contrast, the modified Gram-Schmidt method does not form the Hessian but instead requires $n_Q N^2$ multiplications to evaluate the necessary inner products and $n_Q N^2/2$ multiplications to update the array storing the evaluation of the basis polynomials at the quadrature nodes. For the numerically computed Hessian to have full rank, it is necessary that $n_Q \geq N + 1$. The benefit of using Cholesky increases as n_Q increases.

While the Gram-Schmidt algorithm is somewhat more stable numerically, in our experience, the difference is negligible, partly because when the Cholesky computation is inaccurate, our algorithm (Algorithm 1) automatically reorthogonalizes by recomputing the Cholesky factor. Indeed, suppose the line search fails, that is, at some iteration k , it backtracks all the way to $\beta_{k,\text{out}}$. Since we did not compute the Hessian $H_k(\beta_{k,\text{out}}) = L_k^{-1} H_{k-1}(\beta_{k,\text{out}}) L_k^{-T}$ but rather assumed it was the identity, this may mean that it was not as close to the identity as expected. If we simply let the algorithm proceed to iteration $k + 1$ with $\beta_{k+1,\text{in}} = \beta_{k,\text{out}}$, the next step is to compute $H_k(\beta_{k+1,\text{in}})$. Notice that $H_k(\beta_{k+1,\text{in}}) = H_k(\beta_{k,\text{out}})$ is exactly the matrix we had assumed was identity. Now we actually compute it and its Cholesky factor and then use this new Cholesky factor to define a

⁵For clarity, we use \mathbf{p}_{in} to refer to the basis whose evaluations are stored in P_{in} . Actual calculations are performed using P_{in} .

new basis \mathbf{p}_{k+1} —which should be closer to orthonormal—and a new search direction \mathbf{d}_{k+1} . For numerical results see Section 5.1.2, in particular Table 3, below.

Other choices for changing the basis can be generated via the singular value decomposition (SVD). To wit, if $U\Lambda U^T$ is the SVD of $H_{k-1}(\boldsymbol{\beta}_{k,\text{in}})$ and O is any $(N+1) \times (N+1)$ orthogonal matrix, then $L_k = U\Lambda^{1/2}O^T$ satisfies (15). (For example, the choice $O = U$ makes L_k the symmetric square root of $H_{k-1}(\boldsymbol{\beta}_{k,\text{in}})$.) We have found that the change-of-basis defined using Cholesky factorization performs just as well as that defined by the SVD with $O = I$ in the sense that the number of problems solvable without regularization is nearly the same. Therefore, since the SVD gives a non-triangular basis, is more expensive, and is also harder to parallelize, we conclude that the Cholesky factorization is a better choice for our problem.

4.2. Computing the stopping criterion

At each iteration, the two conditions used in the stopping criterion in (16) are computed in the original Legendre basis \mathbf{m} . We use this basis because it is physically relevant for the kinetic equation and using the original basis for flux calculations is simpler to implement in a parallel setting because the adaptive basis varies with each spatial cell.

The calculation of the gradient in the Legendre basis for the stopping criterion can be as simple as $\mathbf{g}(\boldsymbol{\alpha}_k) = T_k \mathbf{g}_k(\boldsymbol{\beta}_{k,\text{out}})$, a calculation that takes only $(N+1)^2$ multiplications. Alternatively, we can compute the gradient by first switching back to the multipliers in the Legendre basis by computing $\boldsymbol{\alpha}_k = S_k^T \boldsymbol{\beta}_{k,\text{out}}$ and then

$$\mathbf{g}(\boldsymbol{\alpha}_k) = \langle \exp(\boldsymbol{\alpha}_k^T \mathbf{m}) \rangle - \mathbf{u}. \quad (27)$$

This computation is significantly more expensive (requiring $(N+1+2n_Q)(N+1)$ multiplications, to leading order, and n_Q exponential evaluations). While in exact arithmetic the results are identical, the latter has the advantage of consistency: the same $\boldsymbol{\alpha}_k$ is used in the computation of the flux in (8).

The estimated upper bound on γ in the stopping criterion (16), whose computation amounts to estimating the maximum value of the polynomial $\mathbf{d}_k(\boldsymbol{\beta}_{k,\text{out}})^T \mathbf{p}_k = \mathbf{d}(\boldsymbol{\alpha}_k)^T \mathbf{m}$, can be computed in either basis. The Newton direction $\mathbf{d}_k(\boldsymbol{\beta}_{k,\text{out}})$ can be converted back to basis \mathbf{m} using T_k to use (19) directly, or we can modify (19) to use the one-norm of $\mathbf{d}_k(\boldsymbol{\beta}_{k,\text{out}})$ and the maximum of the basis polynomials in \mathbf{p}_k on the quadrature nodes, $\max_{ij} |p_i(\mu_j)|$ (see Theorem 1). We chose the former though we did not notice a significant difference between the two options in the performance of the optimizer.

4.3. Returning to the Legendre basis

Solving an optimization problem in a changing basis requires careful bookkeeping. In Algorithm 2 we choose to update both the matrix T_k defining the change of basis and the $(N+1) \times n_Q$ matrix P_k of basis polynomial values at quadrature points, even though it is only strictly necessary to update one of them.⁶

⁶Indeed, at every iteration, each matrix can be obtained from the other ($P_k = T_k^{-1}M$ (where M holds the values of the original basis polynomials \mathbf{m} at the quadrature nodes), and $T_k^{-1} = P_k M^T (M M^T)^{-1}$), and each matrix can be incrementally updated using L_k .

Firstly, we choose to update P_k because it is used repeatedly at each iteration in quadratures during the line search. We choose to update T_k as well (at a cost of N^3 multiplications per iteration) because it makes the computations for the stopping criterion simpler, and this extra cost had negligible effects on the total computation time for our implementation.

4.4. Regularization

The algorithm in [3] deems an optimization problem ‘too difficult’ when the adaptive quadrature routine requires more points to estimate the objective function than a user-prescribed limit. In such cases, the regularization parameter r in (26) is increased.

In Algorithm 1, we instead increase the regularization parameter when the optimization has not converged after k_0 iterations. As a result, in our implementation, regularization is used less frequently than in [3]. As in [3], we assume that r_{\max} , the highest value of r used by the algorithm, is such that all problems can be solved. Therefore, when r reaches r_{\max} , we continue the optimization past k_0 iterations. While we have been able to construct moments for which $r_{\max} = 10^{-4}$ is not large enough to produce a numerically solvable optimization problem (see Section 5.1.2 below), we have never found problems this hard in any of the benchmark simulations, where that value of r_{\max} was used.

5. Numerical Results

In this section we report on a series of numerical experiments we performed to assess the performance of Algorithm 1. These include experiments with (i) static problems for a fixed set of moments, (ii) computation of a manufactured solution, and (iii) the simulation of two well-known benchmark problems in radiative transport.

Unless otherwise noted, we use the following parameter values:

$\tau = 10^{-9}$,	upper bound for $\ \mathbf{g}(\boldsymbol{\alpha}_k)\ $ in the stopping criterion,
$\varepsilon_\gamma = 0.01$,	upper bound on $\gamma_{\max} - 1$ to maintain realizability,
$\theta = 2.0$,	slope limiting parameter,
$\chi = 0.5$,	line search step size decrease parameter,
$\xi = 10^{-3}$,	line search sufficient decrease parameter,
$\{r_\ell\} = \{0, 10^{-8}, 10^{-6}, 10^{-4}\}$	sequence of regularization parameters to try
$k_{\max} = 200$,	maximum number of iterations,
$\varepsilon = 2^{-52}$,	parameter used in line-search termination.

When simulating (8), we set

$$\Delta t = \frac{0.95}{1 + \varepsilon_\gamma} \frac{2}{\theta + 2} \Delta x, \quad (28)$$

which, in view of (20), satisfies the time-step restriction (24).⁷

The initial multipliers for the optimization algorithm at $t = 0$ are those corresponding to the isotropic distribution, $\boldsymbol{\beta}_{0,\text{in}} = (\log(u_0/2), 0, \dots, 0)^T$, and the initial basis for each problem is the Legendre basis \mathbf{m} , so that $T_{-1} = I$, $P_{-1} = M$. At later times we begin each

⁷For all cases considered here $\sigma_t = O(1)$. Thus the effect of σ_t on the CFL condition in (24) is accounted for by the “safety factor” 0.95.

optimization with the final multipliers and basis from the spacial cell's optimization problem at the previous time step. Consequently, T_k is always lower-triangular, allowing us to use the gradient formula in Algorithm 2.

As discussed in Section 3.3, we use Curtis-Clenshaw quadrature to approximate all angular integrals. Following [3], we approximate each half interval $\mu \in [-1, 0]$ and $\mu \in [0, 1]$ separately since (due to upwinding) integrals at cell edges in the numerical scheme have different forms for each half-interval. Except for Section 5.1.1, we use an equal number of quadrature points (i.e. $n_Q/2$) on each half-interval.

5.1. Static Results

We perform two experiments using static problems—that is, problems for which the moments are chosen, as opposed to being generated by the solution of a partial differential equation.

5.1.1. Adaptive vs. Fixed Basis with Different Quadratures

In our first experiment, we use the following M_{15} moment vector that was encountered in [3]:

$$\mathbf{u} = \begin{bmatrix} 1.0, & 0.837872568, & 0.572819692, & 0.294071376, \\ 0.079519254, & -0.034894762, & -0.060428124, & -0.037077987, \\ -0.006145576, & 0.009337451, & 0.007920869, & 0.000075451, \\ -0.004350212, & -0.002832808, & 0.001074657, & 0.003022835 \end{bmatrix}^T \quad (29)$$

to compare the fixed- and adaptive-basis methods. In Figure 2, we show the results from attempting to solve the dual problem with this value of \mathbf{u} using a fixed-basis method (in the Legendre basis) and the adaptive-basis method of Algorithm 1. In each case, the initial multiplier vector corresponds to the isotropic distribution and no regularization is used, i.e. $\{r_\ell\} = \{0\}$. Each square pixel in Figure 2 displays the number of iterations required in Algorithm 1 for a particular choice of quadrature. White pixels indicate that the optimization was unable to converge within 200 iterations.

For the adaptive basis method, the algorithm converges for every tested quadrature with at least 45 nodes on $[-1, 0]$ in 13–64 iterations. This suggests that 45 Curtis-Clenshaw nodes are needed to describe the structure in the ansatz on $\mu \in [-1, 0]$ near the solution $\hat{\alpha}$. The fixed basis method, on the other hand, is highly unpredictable and frequently does not converge within 200 iterations.

5.1.2. Approaching the Boundary of Realizability

Next we show that, compared to a fixed basis, the adaptive-basis method allows us to solve optimization problems closer to the realizable boundary $\partial\mathcal{R}_m$. For $N \geq 2m$, moments given by

$$\mathbf{u} = \left\langle \mathbf{m} \sum_{i=1}^m c_i \delta(\mu - \nu_i) \right\rangle = \sum_{i=1}^m c_i \mathbf{m}(\nu_i) \quad (30)$$

(where $c_i \geq 0$ and $\nu_i \in [-1, 1]$) lie on $\partial\mathcal{R}_m$ [28]. For $\ell \in \{0, 1, 2, \dots\}$, let $r_\ell = 2^{-\ell}$. Then for any $\mathbf{u} \in \partial\mathcal{R}_m$, the sequence of regularized moments (cf. (26))

$$\mathbf{v}(\mathbf{u}, r_\ell) = (1 - r_\ell)\mathbf{u} + r_\ell Q\mathbf{u}, \quad \ell \in \{0, 1, 2, \dots\}, \quad (31)$$

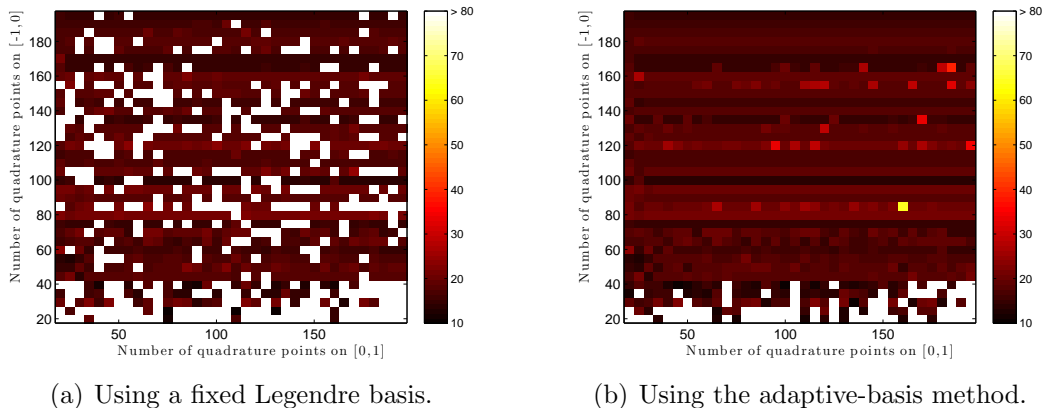


Figure 2: Number of iterations used by the fixed-basis method and the adaptive-basis method on the moments given in (29) using Curtis-Clenshaw quadratures with a varying number of nodes.

approaches $\partial\mathcal{R}_{\mathbf{m}}$ as $\ell \rightarrow \infty$. Let ℓ_A be the largest value of ℓ such that the adaptive-basis method converges with input moment $\mathbf{v}(\mathbf{u}, r_\ell)$ for all $\ell \leq \ell_A$, and let ℓ_F be defined in a similar way for the fixed-basis method. Then r_{ℓ_A} and r_{ℓ_F} give an indication of how much regularization is needed to solve different problems near the realizable boundary.

We performed experiments to compute ℓ_A and ℓ_F with moment vectors of length 13 ($N = 12$) that are generated via (30) using a combination of $m = 6$ delta functions. Table 1 gives the strengths c_i and locations ν_i of the delta functions generating example moments $\mathbf{u}^{(1)}, \dots, \mathbf{u}^{(6)}$, each of which lies on $\partial\mathcal{R}_{\mathbf{m}}$. The moments $\mathbf{u}^{(1)}, \dots, \mathbf{u}^{(4)}$ are chosen to show the effects of changing the strengths c_i and the distance between locations of the delta functions, while $\mathbf{u}^{(5)}$ and $\mathbf{u}^{(6)}$ are chosen to illustrate the case when quadrature nodes are co-located with the delta functions generating the moments on the boundary. The delta functions generating $\mathbf{u}^{(5)}$ are located at the 4-th, 7-th, 10-th, 13-th, 14-th, and 15-th nodes of the 20-point Curtis-Clenshaw quadrature over the interval $[-1, 0]$; for $\mathbf{u}^{(6)}$, the locations $\nu_1, \nu_3, \nu_4, \nu_5$, and ν_6 correspond to the 4-th, 9-th, 12-th, 15-th, and 17-th nodes, respectively, of the same quadrature, while ν_2 is the 54-th node of the 153-point Curtis-Clenshaw quadrature over the interval $[-1, 0]$.

Values of r_{ℓ_A} and r_{ℓ_F} are displayed in Table 2. These values are computed using several different quadratures sizes. The values of n_Q are chosen so that the quadratures are nested. (The nodes of the Curtis-Clenshaw quadrature of order $2n - 1$ include all nodes of the quadrature of order n .) The table shows that the adaptive-basis method nearly always uses a smaller regularization parameter than the fixed-basis method, in many cases by two orders of magnitude.

We repeated the boundary-moment tests of Table 2 using the modified Gram-Schmidt method instead of Cholesky factorization, in order to assess whether the added stability enables the solution of dual problems for moments closer to the realizable boundary. The results in Table 3 show that the modified Gram-Schmidt algorithm does not provide a significant advantage.

Table 1: Boundary moments used for tests in Table 2 below.

i	1	2	3	4	5	6	
$\mathbf{u}^{(1)}$	ν_i	0.2	0.3	0.4	0.5	0.6	0.7
	c_i	0.167	0.167	0.167	0.167	0.167	0.167
$\mathbf{u}^{(2)}$	ν_i	0.2	0.3	0.4	0.5	0.6	0.7
	c_i	0.0833	0.0833	0.0833	0.333	0.0833	0.333
$\mathbf{u}^{(3)}$	ν_i	0.2	0.4	0.6	0.88	0.89	0.9
	c_i	0.0833	0.0833	0.0833	0.333	0.0833	0.333
$\mathbf{u}^{(4)}$	ν_i	-0.8	-0.5	-0.1	0.59999	0.6	0.8
	c_i	0.167	0.167	0.167	0.167	0.167	0.167
$\mathbf{u}^{(5)}$	ν_i	-0.94	-0.773	-0.541	-0.299	-0.227	-0.161
	c_i	0.417	0.0417	0.0417	0.0417	0.417	0.0417
$\mathbf{u}^{(6)}$	ν_i	-0.94	-0.729	-0.623	-0.377	-0.161	-0.0603
	c_i	0.167	0.167	0.167	0.167	0.167	0.167

Table 2: Values of the smallest regularization parameters giving convergence of Algorithm 1 for the moments in Table 1: r_{ℓ_A} (adaptive basis) and r_{ℓ_F} (fixed basis).

n_Q	$\mathbf{u}^{(1)}$		$\mathbf{u}^{(2)}$		$\mathbf{u}^{(3)}$		$\mathbf{u}^{(4)}$		$\mathbf{u}^{(5)}$		$\mathbf{u}^{(6)}$	
	r_{ℓ_A}	r_{ℓ_F}	r_{ℓ_A}	r_{ℓ_F}	r_{ℓ_A}	r_{ℓ_F}	r_{ℓ_A}	r_{ℓ_F}	r_{ℓ_A}	r_{ℓ_F}	r_{ℓ_A}	r_{ℓ_F}
40	1.5e-5	1.2e-4	1.2e-4	1.2e-4	3.1e-2	3.1e-2	1.2e-1	1.2e-1	3.1e-2	1.5e-5	7.5e-9	6.0e-8
78	1.2e-7	1.2e-7	6.0e-8	1.5e-5	7.6e-6	1.5e-5	1.6e-2	1.6e-2	1.9e-9	3.8e-6	7.5e-9	7.8e-3
154	1.2e-7	1.5e-5	3.0e-8	1.6e-2	2.4e-7	3.8e-6	3.9e-3	1.6e-2	3.0e-8	1.9e-6	7.5e-9	1.5e-5
306	1.2e-7	3.1e-5	1.2e-7	7.6e-6	2.4e-7	1.9e-6	9.8e-4	3.9e-3	2.4e-7	1.5e-5	7.5e-9	1.9e-6
610	1.2e-7	3.1e-5	7.6e-6	9.5e-7	4.8e-7	6.1e-5	2.4e-4	3.9e-3	9.5e-7	2.4e-4	7.5e-9	4.8e-7

Table 3: Same as Table 2 above, but here we compare the use of Cholesky factorization (C) to that of modified Gram-Schmidt (GS) in the adaptive-basis method.

n_Q	$\mathbf{u}^{(1)}$		$\mathbf{u}^{(2)}$		$\mathbf{u}^{(3)}$		$\mathbf{u}^{(4)}$		$\mathbf{u}^{(5)}$		$\mathbf{u}^{(6)}$	
	r_{ℓ_C}	$r_{\ell_{GS}}$	r_{ℓ_C}	$r_{\ell_{GS}}$	r_{ℓ_C}	$r_{\ell_{GS}}$	r_{ℓ_C}	$r_{\ell_{GS}}$	r_{ℓ_C}	$r_{\ell_{GS}}$	r_{ℓ_C}	$r_{\ell_{GS}}$
40	1.5e-5	7.6e-6	1.2e-4	1.2e-4	3.1e-2	3.1e-2	1.2e-1	1.2e-1	3.1e-2	1.2e-10	7.5e-9	7.5e-9
78	1.2e-7	1.2e-7	6.0e-8	6.0e-8	7.6e-6	7.6e-6	1.6e-2	1.6e-2	1.9e-9	9.3e-10	7.5e-9	7.5e-9
154	1.2e-7	1.2e-7	3.0e-8	6.0e-8	2.4e-7	4.8e-7	3.9e-3	3.9e-3	3.0e-8	1.2e-7	7.5e-9	7.5e-9
306	1.2e-7	1.2e-7	1.2e-7	1.2e-7	2.4e-7	1.2e-7	9.8e-4	9.8e-4	2.4e-7	4.8e-7	7.5e-9	7.5e-9
610	1.2e-7	1.2e-7	7.6e-6	1.2e-7	4.8e-7	4.8e-7	2.4e-4	2.4e-4	9.5e-7	4.8e-7	7.5e-9	7.5e-9

5.2. Results on a manufactured-solution testbed

In our third test, we assess the effect of regularization on the accuracy of the solution to the moment system. In general, this is difficult to measure since the true solution is generally unknown, and we are unable to compute high-resolution approximations without regularization. As an alternative, we use the method of manufactured solutions [33, 34]. Following this approach, we solve numerically the system

$$\partial_t \mathbf{u} + \partial_x \mathbf{f}(\mathbf{u}) = \partial_t \mathbf{w} + \partial_x \mathbf{f}(\mathbf{w}), \quad (32)$$

where \mathbf{w} is a specified target solution. For simplicity, we set

$$\mathbf{w}(x, t) := \langle \mathbf{m} \exp(\boldsymbol{\alpha}(x, t)^T \mathbf{m}) \rangle, \quad (x, t) \in [-1, 1] \times [0, t_f], \quad (33)$$

where

$$\alpha_1(x, t) = 0.1 + \frac{K}{2} (\cos(\pi(x - t)) + 1), \quad K > 0, \quad (34a)$$

$$\alpha_0(x, t) = \log \left(\frac{(1 + \frac{1}{2} \cos(\pi(x - t))) \alpha_1(x, t)}{2 \sinh(\alpha_1(x, t))} \right). \quad (34b)$$

and $\alpha_2(x, t) \equiv \alpha_3(x, t) \equiv \dots \equiv \alpha_N(x, t) \equiv 0$, so that integrals of the form $\langle \mu^k \exp(\boldsymbol{\alpha}^T \mathbf{m}) \rangle$ can be computed explicitly. In particular,

$$w_0(x, t) = 1 + \frac{1}{2} \cos(\pi(x - t)). \quad (35)$$

It is clear from (34a) that α_1 is always positive, which means that particles are always moving to the right. Meanwhile, the parameter K controls the distance between \mathbf{w} and $\partial \mathcal{R}_{\mathbf{m}}$. Indeed, as K increases, the ansatz $G_{\hat{\alpha}(\mathbf{w})}$ looks more and more like a single delta function at $\mu = 1$, particularly when $x = t$, where $\alpha_1(x, t)$ reaches its maximum. The offset value 0.1 is included in (34a) order to bound α_1 away from zero, where the exact evaluation of integrals of the form $\langle \mu^k \exp(\alpha_1 \mu) \rangle$ is numerically unstable. The profile of the particle density u_0 is

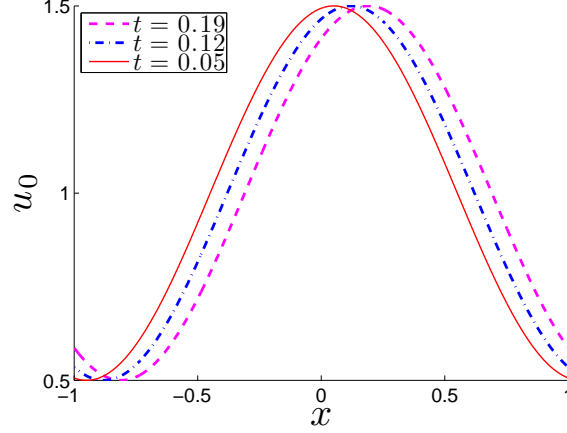


Figure 3: The particle density $u_0(x, t)$ for the manufactured-solution system (32)-(34b) with M_3 and $K = 10$, computed using $N_x = 800$ cells.

plotted at a few different times in Figure 3. For the errors and statistics presented below, we use $N = 3$, $K = 10$, and $t_f = 0.2$.

The kinetic scheme requires cell averages of the known right-hand side of (32). This requires the integral of $\partial_t \mathbf{w}$ over I_j as well as pointwise evaluation of the flux $\mathbf{f}(\mathbf{w}(x, t)) = \langle \mu \mathbf{m} \exp(\boldsymbol{\alpha}(x, t)^T \mathbf{m}) \rangle$ at cell edges. For the target solution in (33), the integral of $\partial_t \mathbf{w}$ does not have an analytical form, so we approximate it using 16-point Curtis-Clenshaw quadratures on $(x_{j-1/2}, x_{j+1/2})$. Periodic boundary conditions are enforced using ghost cells.

Having the exact solution $\mathbf{w}(x, t)$ allows us to calculate errors for every numerical simulation. We first interpolate the cell averages using second-order affine reconstructions in each spatial cell:

$$\mathbf{u}_{\Delta x}(x) = \mathbf{u}_j + (x - x_j) \frac{\mathbf{u}_{j+1} - \mathbf{u}_{j-1}}{2\Delta x}, \quad x \in I_j, \quad j \in \{1, \dots, N_x\}, \quad (36)$$

where the moments are all taken at time t_f . Then the L^1 and L^∞ errors are given as

$$\mathbf{e}_{\Delta x}^1 := \int_{-1}^1 |\mathbf{w}(x, t_f) - \mathbf{u}_{\Delta x}(x)| dx \quad \text{and} \quad \mathbf{e}_{\Delta x}^\infty := \max_{x \in [-1, 1]} |\mathbf{w}(x, t_f) - \mathbf{u}_{\Delta x}(x)|, \quad (37)$$

respectively, where the absolute value is taken component-wise. To approximate the integral in $\mathbf{e}_{\Delta x}^1$, we split each spatial cell I_j into 100 equally sized subintervals, and then apply a twenty-point Gaussian quadrature on each subinterval. We approximate $\mathbf{e}_{\Delta x}^\infty$ with the maximum value of $|\mathbf{w}(x, t_f) - \mathbf{u}_{\Delta x}(x)|$ over those same quadrature points. Below, we only report errors in the particle density u_0 , i.e. the zero-th component of $\mathbf{e}_{\Delta x}^1$ and $\mathbf{e}_{\Delta x}^\infty$. For $q \in \{1, \infty\}$, the order of convergence ν between two successive grids of size Δx_1 and Δx_2 is defined by the equality

$$\mathbf{e}_{\Delta x_2}^q / \mathbf{e}_{\Delta x_1}^q = (\Delta x_2 / \Delta x_1)^\nu, \quad (38)$$

where all operations are performed component-wise.

We now use the manufactured solution to compare the adaptive- and fixed-basis methods. The results of Section 5.1 suggest that less regularization is needed with the adaptive-basis

Table 4: Manufactured solution: Use of regularization for adaptive-basis with $n_Q = 40$ (AB-Q40), fixed-basis with $n_Q = 40$ (FB-Q40), and fixed-basis with $n_Q = 240$ (FB-Q240). Recall that E is defined in (39).

N_x	fraction regularized			mean r			E		
	AB-Q40	FB-Q40	FB-Q240	AB-Q40	FB-Q40	FB-Q240	AB-Q40	FB-Q40	FB-Q240
100	4.55e-04	6.14e-03	4.32e-03	4.35e-12	4.89e-10	9.02e-10	8.89e-08	9.78e-06	1.82e-05
200	7.67e-03	2.99e-02	2.97e-02	5.25e-10	5.02e-09	5.47e-09	4.09e-05	3.85e-04	4.18e-04
400	6.98e-04	6.37e-03	6.90e-03	3.53e-11	5.32e-10	2.03e-09	1.06e-05	1.36e-04	4.76e-04
800	4.24e-04	2.72e-03	2.63e-03	5.10e-11	5.74e-10	5.87e-10	6.30e-05	7.09e-04	7.25e-04
1200	6.77e-04	4.09e-03	3.96e-03	5.65e-11	8.63e-10	9.05e-10	1.57e-04	2.39e-03	2.51e-03
1600	8.60e-04	5.27e-03	5.20e-03	9.63e-11	1.16e-09	1.13e-09	4.74e-04	5.72e-03	5.53e-03
2000	1.08e-03	6.62e-03	6.36e-03	1.12e-10	1.50e-09	1.38e-09	8.57e-04	1.15e-02	1.06e-02

method. Because regularization introduces errors, we expect the adaptive-basis solution to be more accurate. To test this hypothesis, we consider three cases: the adaptive-basis method with $n_Q = 40$ quadrature points (AB-Q40), the fixed-basis method with $n_Q = 40$ quadrature points; (FB-Q40); and the fixed-basis method with $n_Q = 240$ quadrature points (FB-Q240). In all three cases, we use Curtis-Clenshaw quadrature and a regularization parameter $k_0 = 40$.

We first examine the difference in regularizations needed by each method. Table 4 shows (i) the fraction of problems regularized, (ii) the average regularization parameter, and (iii) the statistic

$$E := \sum_{n=0}^{N_t-1} \sum_{m=1}^2 \sum_{j=1}^{N_x} r_j^{n,m} u_{j,0}^{n,m}, \quad (39)$$

where $r_j^{n,m}$ is the value of r used by the optimization algorithm in cell j at time $t^n = n\Delta t$ and Runge-Kutta stage m , and $u_{j,0}^{n,m}$ is the corresponding cell average of the particle density u_0 . Within a single cell, the L^1 -norm of the error introduced by regularization is bounded by rNu_0 , since (see (26))

$$\|\mathbf{u} - \mathbf{v}(\mathbf{u}, r)\|_1 = r \|Q\mathbf{u} - \mathbf{u}\|_1 = r \|(0, -u_1, \dots, -u_N)^T\|_1 \leq rNu_0, \quad (40)$$

where we have used the fact that, since $\|m_i\|_\infty = 1$, $|u_i| \leq u_0$ for $i \in \{1, \dots, N\}$. Thus E gives us an estimate of the error introduced by regularization. By each of these three metrics, the adaptive-basis method uses less regularization than either fixed-basis method.

In Table 5, we show L^1 and L^∞ errors for each method. Along with the results in Table 4, these errors suggest the following conclusions:

1. **The regularization causes the convergence to slow significantly.** While a different regularization strategy might improve these results, we expect that both adaptive-basis and fixed-basis methods will eventually stall. This is because it is not possible to scale the regularization with the mesh. Indeed in many problems, the optimization may become more difficult as the mesh is refined.

Table 5: Manufactured solution: Convergence in space of L^1 and L^∞ errors for adaptive-basis and fixed-basis optimization methods. Errors are only computed for u_0 .

N_x	AB-Q40		FB-Q40		FB-Q240	
	L^1	ν	L^1	ν	L^1	ν
100	5.63e-04	—	5.63e-04	—	5.60e-04	—
200	1.33e-04	2.08	1.33e-04	2.08	1.32e-04	2.09
400	3.11e-05	2.09	3.14e-05	2.08	3.26e-05	2.02
800	7.27e-06	2.10	9.02e-06	1.80	9.12e-06	1.84
1200	3.58e-06	1.74	9.75e-06	-0.19	9.92e-06	-0.21
1600	3.11e-06	0.49	1.40e-05	-1.27	1.32e-05	-0.99
2000	2.83e-06	0.43	1.79e-05	-1.09	1.73e-05	-1.22

	L^∞	ν	L^∞	ν	L^∞	ν
100	1.84e-03	—	1.84e-03	—	1.85e-03	—
200	7.75e-04	1.25	7.66e-04	1.26	7.47e-04	1.30
400	2.72e-04	1.51	2.79e-04	1.46	2.77e-04	1.43
800	8.35e-05	1.70	1.04e-04	1.42	1.03e-04	1.43
1200	4.86e-05	1.33	1.36e-04	-0.66	1.14e-04	-0.26
1600	3.73e-05	0.92	1.67e-04	-0.72	1.66e-04	-1.31
2000	3.38e-05	0.45	2.31e-04	-1.44	2.10e-04	-1.05

2. **The adaptive-basis method shows better convergence properties.** Even when the convergence is not second-order, the adaptive-basis method has smaller error and higher order of convergence. This is to be expected since the adaptive-basis method regularizes less and the values of the regularization parameter are smaller. Indeed, the convergence of the fixed-basis method stalls around 1200 cells, while the adaptive-basis continues to converge (albeit slowly) up to 2000 cells (the finest mesh). This translates to an error that is a factor of eight smaller at 2000 cells.
3. **More quadrature points do not improve the fixed-basis method.** Increasing the number of quadrature points in the fixed-basis method from 40 to 240 does nothing to improve the convergence. In addition, we have tried using the adaptive-quadrature routine from [3], which refines the quadrature used to evaluate the dual objective function until the tolerance on a specified accuracy criterion is met. However, even with a tolerance of 10^{-13} , the adaptive-quadrature routine never refines the 40-point quadrature. Thus the numerical results are the same as for FB-Q40, but the cost is much higher.

Finally, Table 6 shows CPU times and mean iteration counts. While the iteration counts are roughly the same for all, the CPU times for AB-Q40 are 25% – 30% larger than the times for FB-Q40. We attribute this difference to the more expensive stopping criterion and extra

Table 6: Manufactured solution time and iterations for adaptive-basis with $n_Q = 40$ (AB-40), fixed-basis with $n_Q = 40$ (FB-40), and fixed-basis with $n_Q = 240$ (FB-Q240).

N_x	CPU time (s)			mean iterations		
	AB-Q40	FB-Q40	FB-Q240	AB-Q40	FB-Q40	FB-Q240
100	7.72e+00	6.28e+00	7.17e+00	2.45	2.46	2.46
200	4.31e+01	2.73e+01	3.13e+01	2.73	2.57	2.58
400	1.07e+02	8.60e+01	1.02e+02	2.04	2.05	2.06
800	3.58e+02	2.83e+02	3.24e+02	1.52	1.52	1.52
1200	8.20e+02	6.42e+02	7.39e+02	1.53	1.53	1.53
1600	1.48e+03	1.15e+03	1.31e+03	1.54	1.53	1.53
2000	2.35e+03	1.80e+03	2.05e+03	1.55	1.54	1.54

matrix computations (for example, updating the basis polynomials) in the adaptive-basis method. The CPU times for FB-Q240 are roughly 10% less than the times for AB-Q40. We expect that adding even more quadrature will eventually produce a more expensive method, even though the convergence behavior will not improve.

From the results in this section we conclude that the adaptive-basis, fixed-quadrature method, while more expensive than a fixed-basis, fixed-quadrature method, reduces the need for regularization, thereby allowing further convergence before regularization errors dominate. We also see, from the results using a fixed-basis, fixed-quadrature method with a much higher-order quadrature, that simply adding quadrature points is not as effective at reducing the need for regularization.

5.3. Results on standard test problems

We now revisit the two standard test problems considered in [3, 24]. Throughout, we use $n_Q = 40$. We consider two values of k_0 , the number of iterations of Algorithm 1 before regularization is increased. We use $k_0 = 6$ to illustrate a more aggressive regularization scheme, and $k_0 = 40$ to illustrate a less aggressive regularization scheme. One would expect a more aggressive regularization scheme to introduce more errors due to regularization, but also to solve the problem more quickly since fewer iterations may be used.

5.3.1. Plane-source problem

In this problem, we model particles in an infinite domain with a purely scattering medium $\sigma_t = \sigma_s = 1$. We consider an initial condition

$$\mathbf{u}(x, 0) = \delta(x) + 2F_{\text{floor}} , \quad (41)$$

where $F_{\text{floor}} = 0.5 \times 10^{-8}$ is used to keep moments away from the realizable boundary. Although the problem is posed on an infinite domain, a finite domain is required for practical computation and boundary conditions must be specified. As in [24, 3], we approximate the infinite domain by the interval $[x_L, x_R] = [-D/2, D/2]$, where $D := 2t_f + 0.2$ is chosen to

ensure that the boundary has negligible effects on the solution. At the right and left ends of the boundary, we enforce the boundary conditions

$$\mathbf{u}(x_L, t) = \mathbf{u}(x_R, t) = 2F_{\text{floor}} \quad (42)$$

for $t \geq 0$.

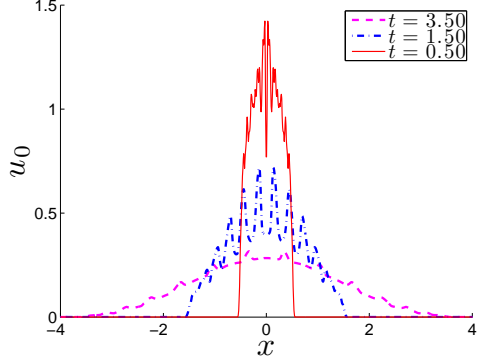
In Figure 4 we present results from a $N_x = 1000$ cell simulation of the M_{15} system with the adaptive-basis method and $k_0 = 6$. The corresponding figures for simulations using $k_0 = 40$ or the fixed-basis method are qualitatively similar. Sample profiles of the resulting particle density $u_0(x, t)$ presented in Figure 4(a) agree with what was presented in [24, 3]. Figure 4(b) shows the iteration profile. The mean number of iterations, excluding trivially solvable isotropic problems, was about 2.03 for $k_0 = 6$, while for $k_0 = 40$ that mean was 2.02. The iteration histogram in Figure 4(c) shows that indeed nearly 99% of the optimization problems were solved in three iterations or fewer with $k_0 = 6$. Figure 4(d) shows the points in space-time where moments were regularized. These moments were encountered as particles from the boundary push out into the vacuum along the front $x = \pm t$ for $t > 0$.

Figure 5 shows a histogram of the regularization parameter r . For the adaptive basis, only 0.36% of the nontrivial optimization problems⁸ were regularized when $k_0 = 6$ and only 0.066% when $k_0 = 40$. The figure also includes the statistics from simulations using the fixed-basis method: when $k_0 = 6$, the results were similar, but when $k_0 = 40$, more regularization was needed than when using the adaptive basis. All results are a significant improvement over [3], where the algorithm regularized about 2.25% of the problems. This is due, in large part, to the change in regularization strategy: In [3], regularization is applied when an adaptive quadrature routine cannot satisfy a prescribed tolerance. Here we instead regularize after a prescribed number of iterations, and this turns out to be a less aggressive strategy.

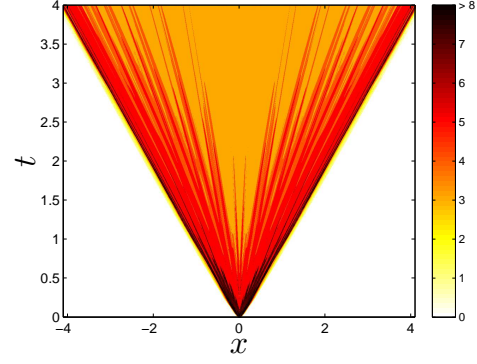
Figure 6 shows the relative differences between the solutions using the two different regularization-scheme parameters, $k_0 = 6$ and $k_0 = 40$, with both adaptive- and fixed-basis methods. The figures show that the biggest differences appear just as the particles enter the surrounding vacuum. In each case, the signs of the errors indicate that the solution computed using less regularization is larger at these points. This indicates that the solution with this scheme is advancing slightly faster, though we note that this difference decreases with time when comparing regularization parameters. When comparing basis methods, the relative errors are a few orders of magnitude smaller.

In Figure 7 we compare more closely the iteration histograms of adaptive- and fixed-basis methods. In a parallel implementation, optimization problems requiring many iterations become a bottleneck, so an optimizer that needs fewer iterations has a significant advantage. However, the results here show that the iteration histograms are nearly identical. This is consistent with our numerical experience that when both methods can solve a problem, they typically take the same number of iterations. (The figure does not include a few outlying problems from the adaptive basis: with $k_0 = 40$, one problem took 529 iterations and three took 530 iterations; with $k_0 = 6$, one problem took 446 iterations and one took 448 iterations.)

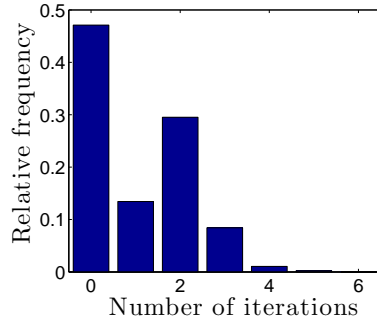
⁸Isotropic moments are not included in the statistics since the optimization is trivial in this case.



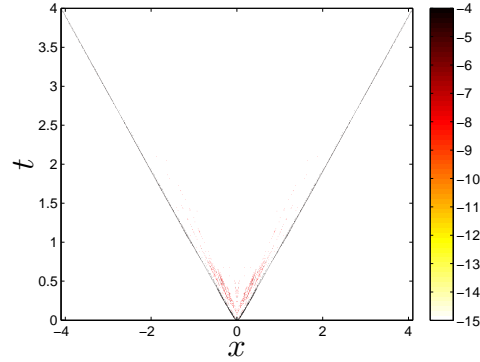
(a) Snapshots of the particle density $u_0(x, t)$ at $t = 0.5, 1.5$, and 3.5 .



(b) The total number of iterations (over the two Runge-Kutta stages) needed to solve the optimization problem at each point in space and time. The maximum number of iterations needed for one time step was 454 (off scale).



(c) A histogram of number of iterations needed to solve each optimization problem. About 0.36% of the problems needed more six iterations.



(d) The locations of regularizations.

Figure 4: Results for the M_{15} model of the plane-source problem using the adaptive-basis method with $k_0 = 6$ and $N_x = 1000$ spatial cells. For this simulation, excluding trivial cases such as cells with isotropic distributions, the optimization problem is solved about 1.1×10^6 times.

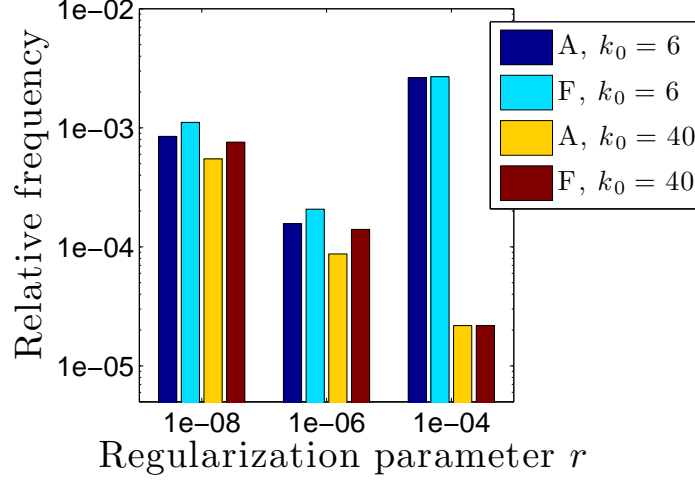
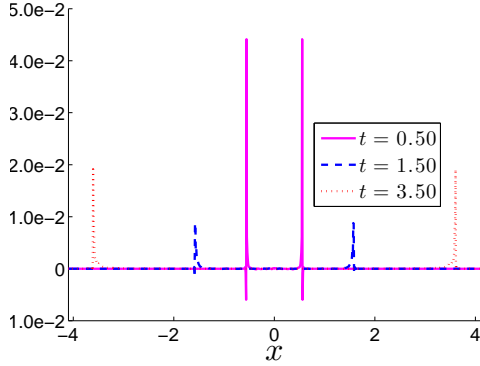
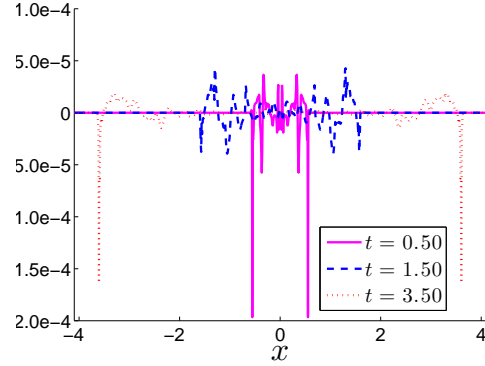


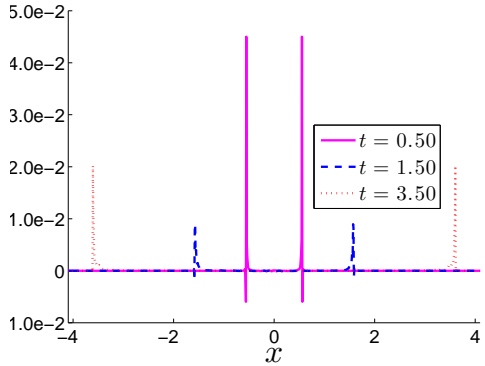
Figure 5: Regularization for the plane source problem.



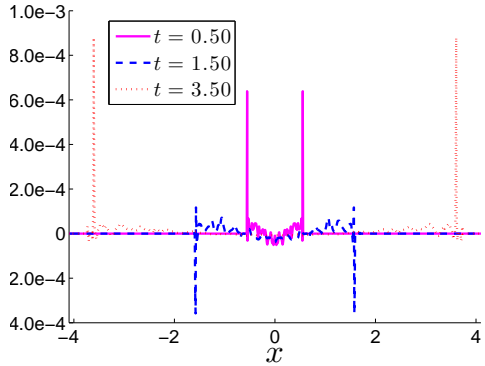
(a) $k_0 = 40$ vs. $k_0 = 6$ with the adaptive basis.



(b) Adaptive vs. fixed basis with $k_0 = 40$.



(c) $k_0 = 40$ vs. $k_0 = 6$ with the fixed basis.



(d) Adaptive vs. fixed basis with $k_0 = 6$.

Figure 6: Relative differences between plane-source solutions. To compare $u_0^{(1)}$ vs. $u_0^{(2)}$ we plot $(u_0^{(1)} - u_0^{(2)}) / (0.5(u_0^{(1)} + u_0^{(2)}))$.

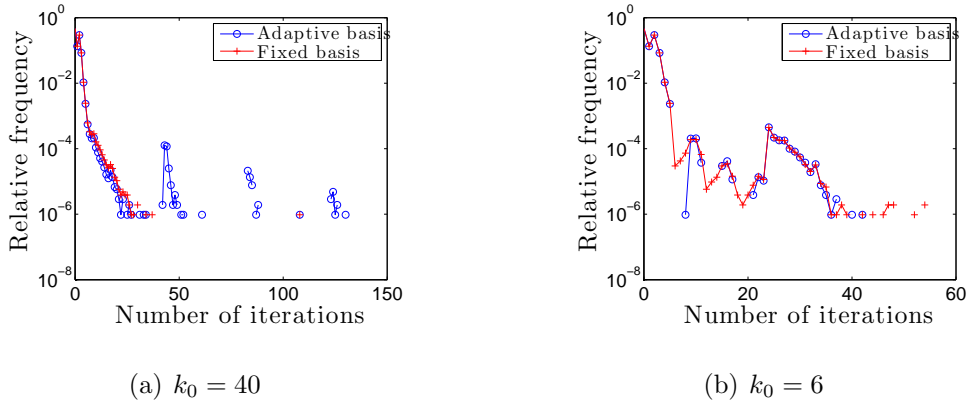


Figure 7: Comparing iteration histograms between adaptive- and fixed-basis methods on the plane-source problem.

5.3.2. Two-beam instability

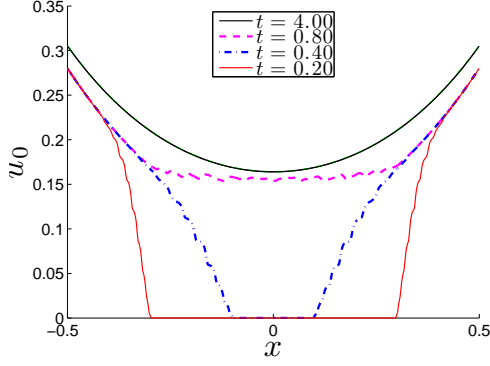
In this problem, particles constantly stream into the domain from the left at $x_L = -0.5$ and the right at $x_R = 0.5$ into the initially (almost) vacuous interior. There is no scattering: $\sigma_s = 0$, while $\sigma_t = 2$. We use ‘forward-peaked’ boundary conditions,

$$\mathbf{u}(x_L, t) = \langle \mathbf{m} \exp(-10(\mu - 1)^2) \rangle, \quad \mathbf{u}(x_R, t) = \langle \mathbf{m} \exp(-10(\mu + 1)^2) \rangle. \quad (43)$$

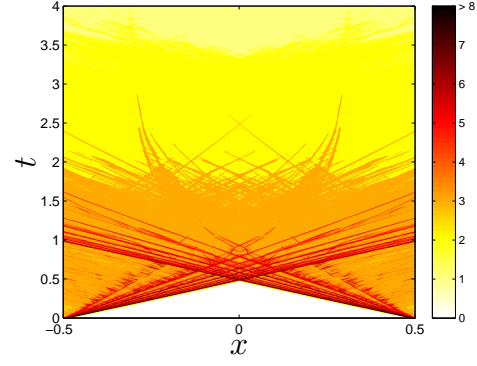
On the interior, the initial condition is isotropic with $u_0(x, 0) \equiv F_{\text{floor}} \langle 1 \rangle$.

Figure 8 presents results from a $N_x = 1000$ cell simulation of the M_{15} system. For this figure we have again used the adaptive-basis method and $k_0 = 6$, but the corresponding figures using $k_0 = 40$ or the fixed-basis method are qualitatively similar. The difference between the final solutions at steady-state using these two different pairs of parameters values is $O(10^{-6})$ in the L^∞ -norm. The transient profile of the particle density $u_0(x, t)$ is shown in Figure 8(a), where we can also see that the steady-state is qualitatively indistinguishable from the steady-state particle density of the kinetic system. These results again agree qualitatively with what was presented in [3, 24]. Figure 8(b) shows the iteration profile. The mean number of iterations (excluding trivially solvable isotropic problems and cells which had already converged) was about 1.37 for $k_0 = 6$, while for $k_0 = 40$ that mean was 1.43. The iteration histogram in Figure 8(c) shows that indeed about 99% of the optimization problems are solved in three iterations or fewer with $k_0 = 6$. (With $k_0 = 40$, about 98% are solved in three iterations or fewer.) Finally, Figure 8(d) shows that regularization occurred mostly where particles from the boundary push into the interior vacuum along the front $x = \pm 0.5 \mp t$ for $t \in [0, 0.5]$.

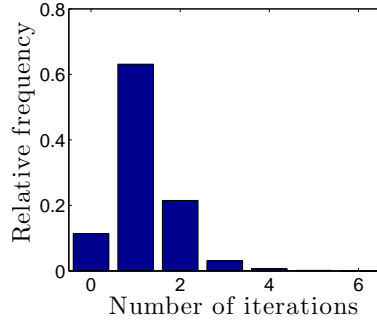
The histogram in Figure 9 shows that the values of the regularization parameter r used for all nontrivial optimization problems are similar to those for the plane-source simulations. For the adaptive basis, about 0.12% of the problems were regularized with $k_0 = 6$ and about 0.087% of the problems were regularized with $k_0 = 40$, with smaller values of r . The fixed-basis method, on the other hand, used significantly more regularization for both values of k_0 . Again, the amount of regularization in all cases is significantly less than in [3], where roughly 1.3% of the problems were regularized.



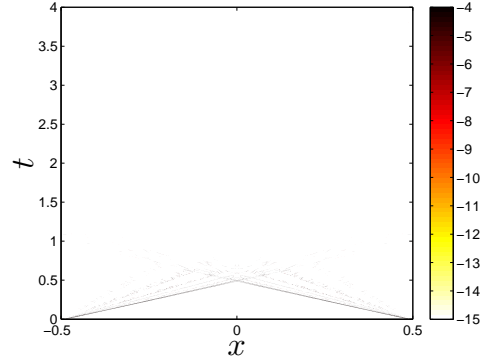
(a) Snapshots of the solution, $u_0(x, t)$ at $t = 0.2, 0.4, 0.8$, and 4 . A green curve shows the true steady-state solution, which is qualitatively indistinguishable from the numerical moment solution at $t = 4$.



(b) The total number of iterations (over the two Runge-Kutta stages) needed to solve the optimization problem at each point in space and time. The maximum number of iterations needed for one time step was 70 (off scale).



(c) A histogram of number of iterations needed to solve each optimization problem. About 0.13% of the nontrivial problems needed more than six iterations.



(d) The locations of regularizations.

Figure 8: Results for the M_{15} model of the two-beam instability with $N_x = 1000$ cells for $k_0 = 6$. For this simulation, excluding trivial cells, the optimization problem is solved about 15×10^6 times.

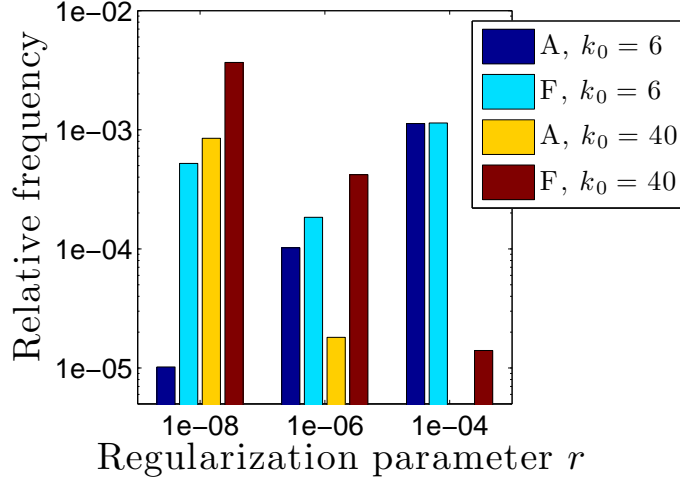
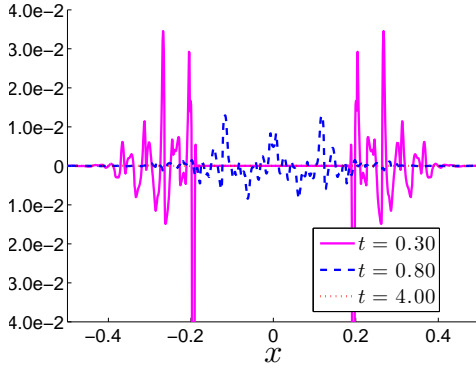
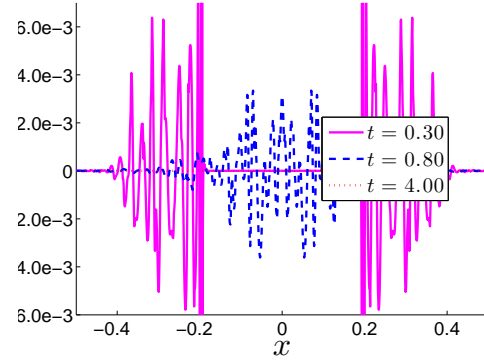


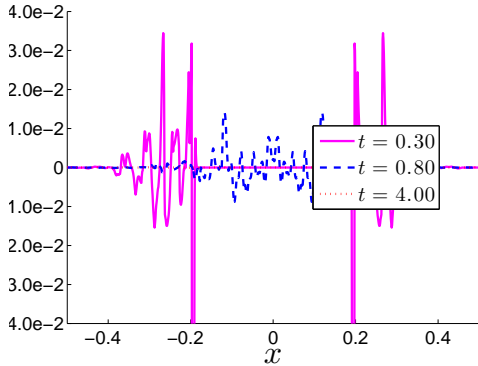
Figure 9: Regularization for the two-beam problem.



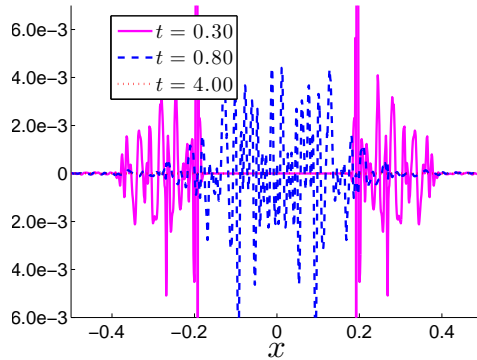
(a) $k_0 = 40$ vs. $k_0 = 6$ with the adaptive basis. Off-scale peaks at $t = \pm 0.2$ are $O(1)$.



(b) Adaptive vs. fixed basis with $k_0 = 40$. Off-scale peaks at $t = \pm 0.2$ are $O(100)$.



(c) $k_0 = 40$ vs. $k_0 = 6$ with the fixed basis. Off-scale peaks at $t = \pm 0.2$ are $O(1)$.



(d) Adaptive vs. fixed basis with $k_0 = 6$. Off-scale peaks at $t = \pm 0.2$ are $O(0.1)$.

Figure 10: Relative differences between two-beam solutions: let $u_0^{(1)}$ and $u_0^{(2)}$ represent the particle densities for the solutions from two different methods. Above we plot $(u_0^{(1)} - u_0^{(2)}) / (0.5(u_0^{(1)} + u_0^{(2)}))$.

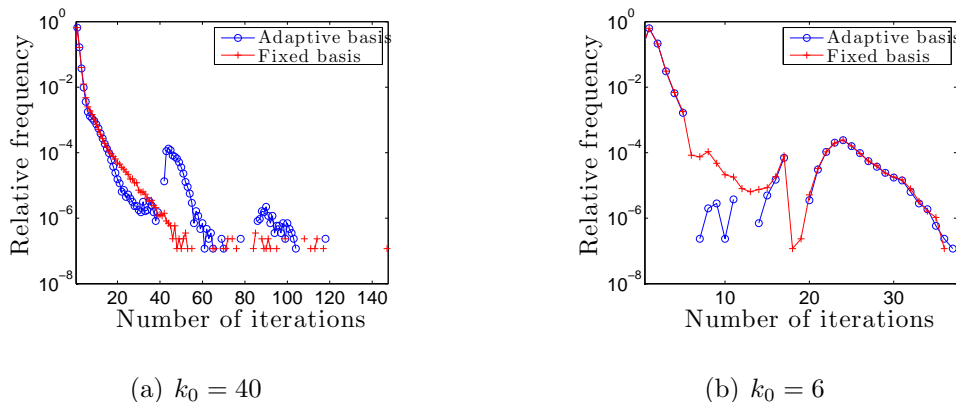


Figure 11: Comparing iteration histograms between adaptive- and fixed-basis methods on the two-beam problem.

Figure 10 shows the relative difference in the solutions from the two different regularization schemes with both basis methods. The results here are not as easily interpreted as in the plane source problem. For $t = 0.3$, the sign of the largest two peaks indicate that the solution with more aggressive regularization has advanced more quickly, but again for later time, these differences decrease.

In Figure 11 we again compare more closely the iteration histograms of adaptive- and fixed-basis methods. Unlike in the plane-source problem, here with $k_0 = 40$ the adaptive-basis optimizer uses a high number of iterations on significantly more problems. This is clearly a consequence of our fairly rudimentary regularization scheme: indeed, notice the increases in histogram near 40 and 80 iterations for the adaptive-basis method in Figure 11(a). They exactly lie where the regularization scheme increases r . On the other hand, with the fixed-basis method, r is often increased before k_0 iterations have passed because the condition number of the Hessian becomes unacceptably high. With adaptive-basis, the condition number of the Hessian stays close to one.

6. Conclusions

We have presented a complete and practical numerical algorithm for solving the M_N entropy-based moment closure model in slab geometry. For the optimization at each space-time grid point, our method uses a change of polynomial basis to keep the Hessian matrix near the identity. This method is closely related to that presented in [13], although we have used the Cholesky factorization instead of the Gram-Schmidt method to define the change of basis. This former is more efficient and, in a series of tests, has been shown to perform comparably. We tested our method on challenging test problems including a new set of manufactured solutions as well as the standard plane source and two-beam problems. Numerical results indicate that the new method has many advantages over the use of a fixed basis such as Legendre polynomials. First, the adaptive basis allows solution of optimization problems closer to the boundary of realizability. This leads to a decreased use of regularization. We show, using the manufactured solution, that regularization introduces errors which can significantly slow or even stall convergence. Therefore, the decreased use of regularization

observed with the adaptive-basis method leads to improved accuracy. Finally we show that the adaptive-basis method performs better with low-resolution quadrature than a fixed-basis method with high resolution quadrature. Thus we can avoid the use of adaptive quadrature (an alternative to improve conditioning of the Hessian), and by using a fixed quadrature the numerical solution remains in a constant computational region of realizability.

Of course, the one-dimensional kinetic model here is simply a testbed. Real problems of practical interest are in two and three dimensions in space and velocity, so future work should test these methods there. A parallel implementation is also necessary to fully exploit the advantages of entropy-based moment closures while minimizing the computational burden of the numerical optimization.

References

- [1] G. N. Minerbo, Maximum entropy Eddington factors, *J. Quant. Spectrosc. Radiat. Transfer* 20 (1978) 541–545.
- [2] B. Dubroca, J.-L. Fegas, Étude théorique et numérique d’une hiérarchie de modèles aux moments pour le transfert radiatif, *C.R. Acad. Sci. Paris I.* 329 (1999) 915–920.
- [3] G. W. Alldredge, C. D. Hauck, A. L. Tits, High-order entropy-based closures for linear transport in slab geometry II: A computational study of the optimization problem, *SIAM J. Sci. Comput.* 34 (2012) B361–B391.
- [4] C. D. Levermore, Moment closure hierarchies for kinetic theory, *J. Stat. Phys.* 83 (1996) 1021–1065.
- [5] M. Junk, Domain of definition of Levermore’s five moment system, *J. Stat. Phys.* 93 (1998) 1143–1167.
- [6] M. Junk, Maximum entropy for reduced moment problems, *Math. Models Meth. Appl. Sci.* 10 (2000) 1001–1025.
- [7] C. D. Hauck, C. D. Levermore, A. L. Tits, Convex duality and entropy-based moment closures: Characterizing degenerate densities, *SIAM J. Control Optim.* 47 (2008) 1977–2015.
- [8] J. Schneider, Entropic approximation in kinetic theory, *Math. Model. Numer. Anal.* 38 (2004) 541–561.
- [9] L. R. Mead, N. Papanicolaou, Maximum entropy in the problem of moments, *Journal of Mathematical Physics* 25 (1984) 2404–2417.
- [10] I. Turek, A maximum-entropy approach to the density of states within the recursion method, *Journal of Physics C: Solid State Physics* 21 (1988) 3251.
- [11] M. Abramowitz, I. A. Stegun, *Handbook of Mathematical Functions with Formulas, Graphs, and Mathematical Tables*, 10th ed., National Bureau of Standards, Washington, DC, 1972.

- [12] J. C. Wheeler, Modified moments and Gaussian quadratures, *Rocky Mountain Journal of Mathematics* 4 (1974) 287–296.
- [13] R. V. Abramov, The multidimensional moment-constrained maximum entropy problem: A BFGS algorithm with constraint scaling, *Journal of Computational Physics* 228 (2009) 96–108.
- [14] R. Abramov, The multidimensional maximum entropy moment problem: A review on numerical methods, *Communications in Mathematical Sciences* 8 (2009) 377–392.
- [15] J. Nocedal, S. Wright, *Numerical Optimization*, 2nd ed., Springer, New York, 2006.
- [16] A. Decarreau, D. Hilhorst, C. Lemarchal, J. Navaza, Dual methods in entropy maximization. Application to some problems in crystallography, *SIAM Journal on Optimization* 2 (1992) 173–197.
- [17] A. Vié, F. Laurent, M. Massot, Size-velocity correlations in high order moment methods for polydisperse evaporating sprays: modelling and numerical issues, *J. Comput. Phys.* (2011) 1–32.
- [18] J. Borwein, W. Huang, A fast heuristic method for polynomial moment problems with Boltzmann-Shannon entropy, *SIAM Journal on Optimization* 5 (1995) 68–99.
- [19] W. Huang, Heuristic solutions to polynomial moment problems with some convex entropic objectives, *Numerical Algorithms* 12 (1996) 297–308.
- [20] K. Bandyopadhyay, A. K. Bhattacharya, P. Biswas, D. A. Drabold, Maximum entropy and the problem of moments: A stable algorithm, *Phys. Rev. E* 71 (2005) 057701.
- [21] S.-C. Fang, J. R. Rajasekera, H.-S. J. Tsao, *Entropy Optimization and Mathematical Programming*, Kluwer Academic Publishers, Boston, 1997.
- [22] L. M. Bregman, The relaxation method of finding the common point of convex sets and its application to the solution of problems in convex programming, *USSR Computational Mathematics and Mathematical Physics* 7 (1967) 200–217.
- [23] R. Gordon, R. Bender, G. Herman, Algebraic reconstruction techniques (ART) for three-dimensional electron microscopy and x-ray photography, *Journal of theoretical biology* 29 (1970).
- [24] C. D. Hauck, High-order entropy-based closures for linear transport in slab geometry, *Comm. Math. Sci.* 9 (2011) 187–205.
- [25] E. E. Lewis, J. W. F. Miller, *Computational Methods in Neutron Transport*, John Wiley and Sons, New York, 1984.
- [26] J. A. Shohat, J. D. Tamarkin, *The Problem of Moments*, American Mathematical Society, New York, 1943.

- [27] J. M. Borwein, A. S. Lewis, Duality relationships for entropy-like minimization problems, *SIAM J. Control Optim.* 1 (1991) 191–205.
- [28] R. E. Curto, L. A. Fialkow, Recursiveness, positivity and truncated moment problems, *Houston Journal of Mathematics* 4 (1991) 603–635.
- [29] S. Gottlieb, C.-W. Shu, E. Tadmor, Strong stability-preserving high-order time discretization methods, *SIAM Review* 43 (2001) 89–112.
- [30] L. Armijo, Minimization of functions having Lipschitz continuous first partial derivatives, *Pacific J. Math* 16 (1966) 1–3.
- [31] E. Olbrant, C. Hauck, M. Frank, A realizability-preserving discontinuous Galerkin method for the M1 model of radiative transfer, *Journal of Computational Physics* (2012).
- [32] J. Lyness, When not to use an automatic quadrature routine, *SIAM Review* 25 (1983) 63–87.
- [33] P. Knupp, K. Salari, Code Verification by the Method of Manufactured Solutions, Unlimited Release SAND20001444, Sandia National Laboratory, 2000.
- [34] P. J. Roache, Code verification by the method of manufactured solutions, *J. Fluids Eng.* (2002) 4–10.